

Local Interstellar Medium Kinematics towards the Southern Coalsack and Chamaeleon-Musca dark clouds

W. J. B. Corradi¹, G. A. P. Franco¹, J. Knude²

¹*Departamento de Física - ICEx - UFMG, Caixa Postal 702, 30.123-970 - Belo Horizonte - MG, Brazil*

²*Niels Bohr Institute for Astronomy, Physics and Geophysics – Juliane Maries Vej 30 – DK 2100 – Copenhagen Ø, Denmark*

ABSTRACT

The results of a spectroscopic programme aiming to investigate the kinematics of the local interstellar medium components towards the Southern Coalsack and Chamaeleon-Musca dark clouds are presented. The analysis is based upon high-resolution ($R \approx 60\,000$) spectra of the interstellar Na I D absorption lines towards 63 B-type stars ($d \leq 500$ pc) selected to cover these clouds and the connecting area defined by the Galactic coordinates: $308^\circ \geq l \geq 294^\circ$ and $-22^\circ \leq b \leq 5^\circ$. The radial velocities, column densities, velocity dispersions, colour excess and photometric distances to the stars are used to understand the kinematics and distribution of the interstellar cloud components. The analysis indicates that the interstellar gas is distributed in two extended sheet-like structures permeating the whole area, one at $d \leq 60$ pc and another around 120-150 pc from the Sun. The nearby feature is approaching to the local standard of rest with average radial velocity of -7 km s⁻¹, has low average column density $\log N_{\text{Na I}} \approx 11.2$ cm⁻² and velocity dispersion $b \approx 5$ km s⁻¹. The more distant feature has column densities between $12.3 \leq \log N_{\text{Na I}} \leq 13.2$, average velocity dispersion $b \approx 2.5$ km s⁻¹ and seems associated to the dust sheet observed towards the Coalsack, Musca and Chamaeleon direction. Its velocity is centered around 0 km s⁻¹, but there is a trend for increasing from -3 km s⁻¹ near $b = 1^\circ$ to 3 km s⁻¹ near $b = -18^\circ$. The nearby low column density feature indicates a general outflow from the Sco-Cen association, in agreement with several independent lines of data in the general searched direction. The dust and gas feature around 120 – 150 pc seem to be part of an extended large scale feature of similar kinematic properties, supposedly identified with the interaction zone of the Local and Loop I bubbles. Assuming that the interface and the ring-like volume of dense neutral matter that would have been formed during the collision of the two bubbles have similar properties, our results rather suggest that the interaction zone between the bubbles is twisted and folded.

Key words: Stars: distances - ISM: clouds - ISM: individual objects: Southern Coalsack - Chamaeleon-Musca - Loop I - Local Bubble

1 INTRODUCTION

The present work is part of a comprehensive investigation of the local interstellar medium (ISM) towards the Southern Coalsack and the Chamaeleon-Musca dark clouds. A comparison of the colour excess $E(b - y)$ vs. distance diagrams for the Chamaeleon-Musca complex (Franco 1991) and the Southern Coalsack (Franco 1989) shows remarkable similarities. The jump of the colour excess to higher values occurs approximately at the same distance, and the observed minimum value of this rise is almost the same: $\Delta E(b - y) \approx 0^m.100$. Although the clouds are apart by more than 15° these facts suggested that they might be dense condensations embedded in an extended interstellar structure.

In order to investigate the possible physical association between these two clouds, a new photometric investigation was carried out. The campaign resulted on very precise $wvby\beta$ data for

1017 stars covering these clouds and the connecting area: $307^\circ \geq l \geq 294^\circ$ and $-20^\circ \leq b \leq 5^\circ$ (Corradi & Franco 1995).

Analysis of the colour excess *vs.* distance diagrams for these stars indicated that exists a foreground region with very little reddening ($E(b - y) \approx 0^m.006$), that is bound, at the distance range of 150 ± 30 pc, by a transition region where the colour excesses suddenly increase to a minimum value of $E(b - y) \approx 0^m.050$ for the most diffuse lines of sight and $E(b - y) \approx 0^m.100$ for the densest ones. Beyond this transition region the diagrams suggest the existence of a second low column density volume, as the complete range of colour excess from $\approx 0^m.050$ to $0^m.275$, shown by the stars in the very narrow distance slot centered on 150 pc, remains unchanged for at least another 350 pc (Corradi et al. 1997, hereafter Paper I).

The onset of this minimum colour excess for the whole surveyed area suggests that the obscuring material is distributed in an extended interstellar sheet-like structure. The existence of such an

absorbing feature, at a distance identical to the molecular clouds, also suggests that Coalsack, Chamaeleon and Musca can be dense condensations embedded on the diffuse medium composing the sheet-like feature.

It has been also noted in Paper I that the jump in $E(b - y)$, caused by the dust feature, seems to have a dependence on the galactic latitude that can be represented by $[E(b - y)_{\min}, b] = [0^m 050; 0^\circ] \rightarrow [0^m 100; -8^\circ] \rightarrow [0^m 150; -15^\circ]$. The quoted dependence might indicate, if we postulate that the dust sheet is roughly perpendicular to the galactic plane, that the sheet does not have the same optical thickness, because $E(b - y)_{\min}$ vs. (b) does not follow a simple $E(b - y)\sec(b)$ law. On the other hand, it might also be the result of approaching the tangential point of a warped sheet-like structure with the same column density, curved away from the Sun.

As pointed out in Paper I, when viewed in connection to the other data on the local ISM, the existence of these two low-reddening volumes has led to the idea that the dust sheet could be part of a large scale structure, probably related to the interface of the Local and Loop I Bubbles. Such an interface of dense matter may have resulted from the compression of the ISM by the action of energetic events of the Sco-Cen OB association from the far side (Weaver 1979; Iwan 1980; Crawford 1991; de Geus 1992) and either by a supernova explosion near the Sun or by whatever created the local low density region from the near side (e.g. Cowie & Songaila 1986; Cox & Reynolds 1987; Bochkarev 1987; Frisch & York 1986; Gehrels & Chen 1993; Hartquist 1994; Bruhweiler 1996). If the dust sheet is part of a small bubble, it could be associated to the LCC-shell proposed by de Geus (1992). Note however that Génova et al. (1997) find that gas is moving out from Sco-Cen in the fourth Galactic quadrant, but towards the association in the first quadrant.

Recently, observational evidences of an annular volume of dense neutral matter, that supposedly would have been formed during the collision of the two bubbles, was found on the ROSAT all-sky survey data by Egger & Aschenbach (1995). Remarkably, as noticed by Dame et al. (1987), the molecular gas from $l \approx 360^\circ$ to 290° and $-25^\circ \leq b \leq 25^\circ$ seemingly define a large complex of clouds around 100-150 pc from the Sun, comprising, e.g., ρ Oph, R CrA, G317-4, Musca, Coalsack, Chamaeleon and the Lupus clouds.

In this case a schematic drawing of the interaction zone between the two bubbles and the dark clouds towards the Sco-Cen association would be like Fig. 1. The position and sizes of the dark clouds were obtained from Dame et al. (1987) and the ring-like contours from Egger & Aschenbach (1995). The dashed square delineates the region surveyed in this work.

To investigate the kinematics of the interstellar gas components towards the Coalsack, Chamaeleon and Musca dark clouds we have obtained high-resolution ($R \approx 60\,000$) spectra of the interstellar Na I D absorption lines. From the radial velocities, column densities, velocity dispersions and the known distance of the stars we aim to study the physical association proposed for these clouds.

2 OBSERVATIONS

2.1 The Program Stars

In order to investigate the interstellar gas components towards the Coalsack, Chamaeleon and Musca dark clouds 60 B-type stars covering the area defined by the Galactic coordinates: $308^\circ \geq l \geq$

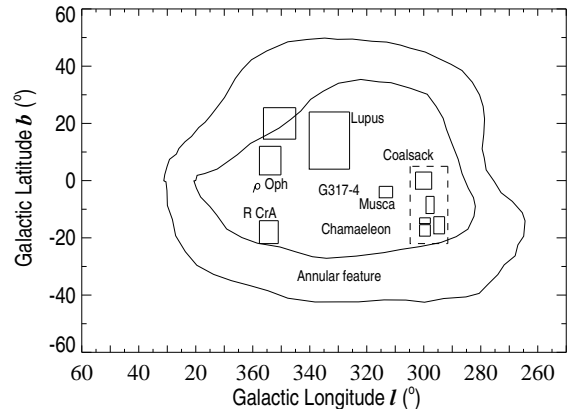


Figure 1. Schematic representation of the interaction zone between the Local and Loop I Bubbles with the dark clouds towards the Sco-Cen association. The position and sizes of the dark clouds were obtained from the survey by Dame et al. (1987). The ring-like contours, taken from the ROSAT all-sky survey data by Egger & Aschenbach (1995), represent the annular volume of dense neutral matter supposedly formed during the collision of the two bubbles. The dashed square delineates the region surveyed in this work

294° and $-22^\circ \leq b \leq 5^\circ$ have been selected from the photometric $wby\beta$ sample by Corradi & Franco (1995). All targets are located within 500 pc from the Sun and have well determined colour excesses $E(b - y)$ and photometric distances (Paper I). SAO 257142, SAO 258697 and PPM 377063 were observed to complement the data at more negative latitudes.

The basic information on the 65 stars is listed in Table 1. For each one the visual magnitude V , the Galactic longitude and latitude, the colour excess and the distance are given in successive columns. Based on the $wby\beta$ data the mean errors in the colour excess and distance values are $0^m 018$ and 15-30%, respectively. The positions of the stars within the surveyed area are given in Fig. 2. The clouds' contours defined by the thick lines are the lowest opacity level of the photographic catalogue by Feitzinger & Stüwe (1984) and the thin one is the outer 2 K km s^{-1} velocity integrated CO emission contour for the Southern Coalsack (Nyman et al. 1989).

The data sample consists of three general divisions based upon the star's location within the area: *inside* the clouds' contours, in their *outskirts* and towards the *sheet-like* structure. They are, respectively, indicated by the (*), (Δ) and (\square) signs. The horizontal and vertical dashed lines delineate eight sub-areas, identified by the roman numbers, that will be used to discuss the details of the velocity structure. Note that 5 stars are within 100 pc, while 7 other are between 100 and 150 pc and another 7 between 150 and 200 pc from the Sun.

2.2 The Instrumental Setup

High resolution ($R \approx 60\,000$) spectra of the Na I D_1 and D_2 absorption lines superposed on the continua spectra of the selected stars have been obtained with the 1.4m Coudé Auxiliary Telescope (CAT) and the Coudé Echelle Spectrometer (CES) at the European Southern Observatory (ESO), in La Silla (Chile). The observations were carried out during 5 nights in April 1996 and 6 nights in April 1997, using the remote control facilities at the ESO's Headquarters in Garching bei München (Germany).

Table 1. Basic information on the program stars

Star	<i>V</i>	<i>l</i> (°)	<i>b</i> (°)	<i>E</i> (<i>b</i> − <i>y</i>)	<i>d</i> (pc)	Star	<i>V</i>	<i>l</i> (°)	<i>b</i> (°)	<i>E</i> (<i>b</i> − <i>y</i>)	<i>d</i> (pc)
Towards the dark clouds contours						Outskirts of the dark clouds					
239370	8.754	294.5	3.1	0.132	427	239779	7.743	298.1	3.6	0.107	468
239702	7.160	297.6	2.6	0.079	379	240265	7.183	302.5	3.2	0.106	489
240621	8.621	305.3	3.0	0.274	454	240368	4.617	303.3	3.7	0.014	136
240645	4.624	305.5	2.8	0.022	65	251460	7.167	295.0	−3.7	0.199	312
251530	8.217	294.7	−0.4	0.105	285	251554	8.215	296.1	−4.2	0.272	291
251545	8.018	295.3	−1.9	0.115	417	251625	7.332	296.9	−3.2	0.149	347
251582	6.880	296.0	−2.7	0.164	291	251717	4.724	297.6	−0.7	0.072	174
251837	7.519	298.9	1.1	0.090	309	251802	7.111	299.2	−3.9	0.103	422
251841	4.053	299.3	−1.3	0.006	99	251894	7.897	300.6	−6.7	0.083	348
251979	8.378	301.3	1.2	0.139	483	251903	4.868	300.1	−0.3	0.015	124
251988	8.838	301.9	−6.8	0.139	402	251928	6.920	300.2	0.8	0.096	313
252114	8.092	303.7	−0.7	0.226	498	251987	6.266	301.7	−3.6	0.021	117
252245	6.674	305.3	−5.7	0.114	123	252262	7.258	305.7	−4.6	0.050	172
252284	4.529	306.7	1.6	0.018	96	252294	7.810	306.0	−4.6	0.108	441
256763	7.978	296.2	−15.8	0.465	229	252321	6.198	306.1	−6.9	0.108	196
256798	7.675	296.6	−14.5	0.220	198	256789	7.970	296.2	−14.1	0.161	227
256849	6.883	297.3	−11.8	0.286	234	256900	8.113	299.3	−9.9	0.194	211
256924	4.240	301.3	−16.5	0.007	86	256980	8.440	302.6	−8.7	0.159	460
256955	3.841	301.4	−9.3	0.003	97	256953	7.777	301.9	−15.3	0.160	284
Towards the sheet											
239327	8.684	294.5	1.6	0.068	500	256828	6.399	295.9	−10.3	0.157	196
239423	8.239	294.8	4.0	0.036	411	256834	5.562	296.3	−10.5	0.192	263
239531	7.455	296.2	2.5	0.056	459	256843	6.079	296.6	−10.6	0.237	135
240041	7.758	300.5	2.8	0.123	231	257002	9.163	303.7	−10.6	0.148	368
251629	8.121	296.2	−0.0	0.105	433	257032	7.628	305.5	−7.8	0.093	284
251699	5.896	298.5	−6.7	0.006	99	257033	6.045	305.3	−9.4	0.145	140
251774	9.160	298.1	0.2	0.107	384	257047	6.618	305.3	−11.9	0.020	175
251874	8.124	300.2	−5.0	0.157	322	257068	8.747	306.3	−10.2	0.126	276
251942	8.072	300.5	1.8	0.094	454	257069	6.308	305.9	−13.0	0.069	149
252136	9.000	304.1	−3.2	0.078	353	257142	5.000	307.0	−18.0	–	169 ^a
256745	5.964	297.1	−18.3	0.076	255	258697	6.800	306.0	−20.3	–	270 ^a
256788	6.759	294.7	−11.1	0.143	190	377063 ^b	5.100	295.0	−21.0	–	165 ^a
256800	5.585	294.5	−9.7	0.106	243						

^a Based on trigonometric parallax from *Hipparcos* (ESA 1997).^b Identification from the PPM catalogue.

The CES optics was optimized to give a reciprocal dispersion of 1.8 Å/mm at the central wavelength of 5890 Å, resulting in a spectral coverage of nearly 60 Å. The entrance slit width of 459 μm, used for all the observations, yielded an actual instrumental resolution (FWHM) $\Delta\lambda = 105 \text{ m}\text{\AA}$ or a velocity resolution $\Delta v = 5.3 \text{ km s}^{-1}$ (FWHM). This corresponds to an actual resolving power of $R \approx 56000$, as determined by measurements of the intrinsic width of the thorium lines.

The CCD was a LORAL/LESSER 2688 x 512, with 16 pre-scan pixels. It has a pixel size of 15 μm × 15 μm and is relatively free of blemishes. Since the optical train selects only a single order, it was always possible to position the spectrum on a clean portion of the CCD. The dark current and the readout noise are very low, 1.8 e^- /pixel/hour at 164 K and 8.3 e^- , respectively. The combined efficiency of the CAT/CES using the long camera is about 8% in the used central wavelength. Additional information regarding the CAT/CES can be found in Kaper & Paquini (1996).

Multiple sets of bias, dark and flat-field exposures were obtained each night for calibration purposes. Exposures of a thorium lamp were taken before and after each object exposure to ensure a better wavelength calibration. The CES, however, showed to be a very stable instrument.

Exposure times ranged from 2 minutes to 2.5 hours, depending on the visual magnitude and spectral type. In all cases signal-to-

noise ratios (S/N) greater than 150 in the raw spectra were achieved. At least two exposures were obtained at each setup position and the integration times were limited to a maximum of 30 minutes to minimize the effects of cosmic ray events in the individual spectra.

2.3 Stellar Distances

Although *Hipparcos* satellite was launched in 1989 August, the catalogue only became available in 1997 (ESA 1997). For this reason, the observing sample was selected based on our photometric distance determination. However, the parallax distances may now serve as a basis for comparison with our photometric distances. A search in the *Hipparcos* catalogue provided us 51 stars in common with our sample – one of them, SAO 239370, appears with negative value for its trigonometric parallax, and was excluded from the comparison. Fig. 3 shows a plot containing the distances based on the *Hipparcos* parallax vs. photometric distances. The denoted errors for the photometric distances were estimated for each star based on the individual uncertainties of their photometric measurements (Corradi & Franco 1995), and ranges from 11 to 49 per cent. In general, the agreement is very good testifying the high quality of our photometric distance determination. There are few stars showing rather large discrepancy between their estimated photometric and parallax distances, usually those beyond 200 pc and

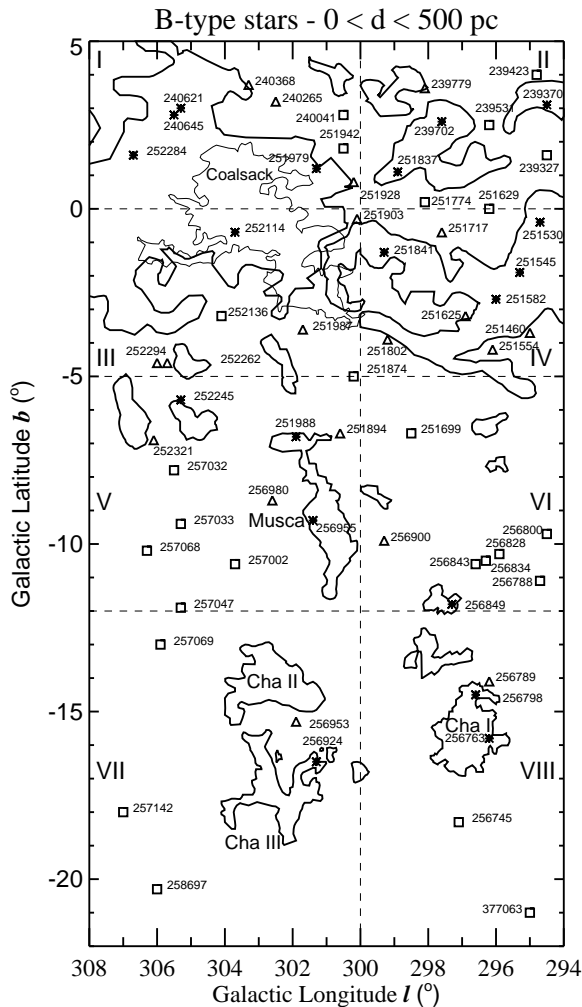


Figure 2. Location of the stars within the studied area. The clouds' contours defined by the thick lines are the lowest opacity level of the photographic catalogue by Feitzinger & Stüwe (1984) and the thin one is the outer 2 K km s⁻¹ velocity integrated CO emission contour for the Coalsack. The (*), (Δ) and (□) signs indicate the stars with line-of-sight *inside* the clouds' contours, in their *outskirts* and towards the *sheet-like* structure, respectively. The horizontal and vertical dashed lines delineate eight sub-areas, identified by the roman numbers, that are used to discuss the details of the velocity structure.

large uncertainties in their trigonometric parallax. However, as will be seen further, the main interstellar structures discussed in this work are located nearer than that, and consequently these uncertainties in the distance estimation do not affect substantially our conclusions.

3 DATA REDUCTION

The initial processing of the CCD frames employed IRAF routines to subtract the bias, divide by a normalized flat-field, and remove cosmic rays from the rows occupied by the stellar spectrum and the background regions. The one-dimensional spectra were then extracted using IRAF routines.

It is worth reiterating that usually the dome flat-fields provided the best correction for the strong vignetting present in the spectra borders, besides that the affected parts were trimmed off

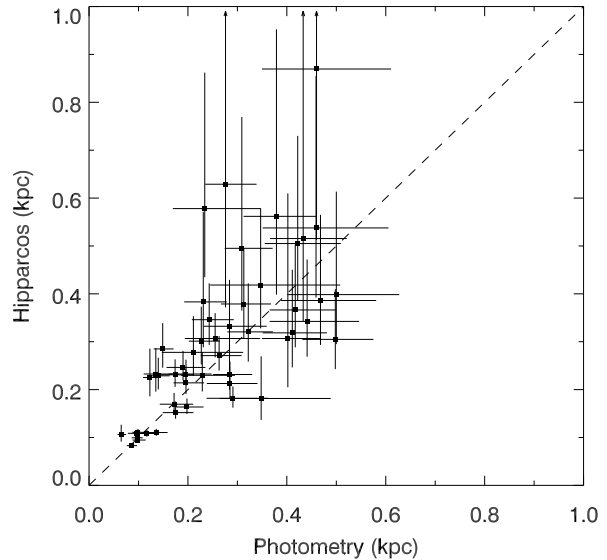


Figure 3. Comparison between the trigonometric distances obtained from the *Hipparcos* catalogue (ESA 1997) and the photometric distances based on *wbyjβ* data.

the images. The wavelength calibration was established with a set of 20 to 30 lines, identified using the thorium line wavelengths of D'Odorico et al. (1987). A second-order Chebyshev function was fitted to the line wavelength as a function of the pixel number, with rms scatter of the residuals about the fit smaller than 0.002 Å (0.05 km s⁻¹) in all cases. The dispersion solution was applied to all science exposures with no rebinning of the data, and the final spectra normalized to unity continuum with cubic splines.

The individual normalized spectra were then co-added on a pixel-by-pixel basis, weighted by the inverse of the rms deviation of the continuum fit. No noticeable degradation in spectral resolution resulted from the co-addition procedure, since the individual spectra have been obtained within an hour or two of each other, and the velocity changes in the observer rest frame, over this time scale, are very small compared to the instrumental resolution.

Numerous absorption lines arising from the Earth's atmosphere occur in this region of the spectrum, and two lines in particular (at 5889.637 Å and 5890.09 Å) are very close to the rest wavelength of the D₂ line. Hobbs (1978) discusses the origin and identification of these atmospheric (telluric) lines in the Na I D wavelength region. To reduce telluric line contamination the stellar spectra were divided out by a purely atmospheric absorption template spectrum obtained from a fast rotating, unreddened early-type star with no interstellar sodium, and taken at similar air mass. For both observing runs spectra of α Leo and γ Lup were taken each night. The equivalent width of the Na I D lines for these stars are estimated to be ≤ 1 mÅ and 1.4 mÅ, respectively (Welsh et al. 1991; Crawford 1991). The stars SAO 251050 and SAO 224833 (ι Lup), initially chosen as candidates for telluric line correction, showed the presence of interstellar Na I D lines.

Since most of the telluric lines arise from water molecules, their strengths change throughout the night as the water content of the Earth's atmosphere changes. Hence, the template spectra were properly scaled to match the strengths of the atmospheric lines in the object spectra. The success of the atmospheric correction procedure is apparent from the fact that all the telluric lines, which are

clear of the interstellar lines, have been satisfactorily removed (see Fig. 4).

Finally the observed wavelengths were brought to the velocity scale and converted to the Local Standard of Rest (LSR) velocity frame, assuming a solar motion of 20 km s^{-1} towards $\alpha = 18^{\text{h}}$ and $\delta = 30^{\circ}$ (Mihalas & Binney 1981). To access the zero point of the velocities the wavelengths of some of the numerous telluric lines gathered in the observed spectral range were measured, providing an external accuracy of the order of $4 \text{ m}\text{\AA}$ and showing that the lines match quite well, seemingly with no systematic offset.

4 THE ABSORPTION-LINE PROFILES

All observed absorption lines show appreciable velocity structure, and thus profile fitting provides the best method for determining accurate interstellar column densities as well as to discern and determine the properties of the individual interstellar clouds contributing to the line profile. The observed profiles of the D_2 and D_1 absorption-lines are shown in Fig. 4. The dots represent the object spectra and the solid line gives the adopted multicomponent fit, as described below. The line-fitting program (FITS6P) has been kindly provided to us by Dr. Welty. Further details of the employed method can be found in Welty et al. (1994) and Sembach et al. (1993). The zero point of the velocities in the upper and lower panels are with respect to the rest wavelength of the D_2 (5889.9510 \AA) and D_1 (5895.9242 \AA) lines, respectively. In each panel the tick marks and numbers above the profiles identifies the different components used to fit the D_2 and D_1 lines.

Voigt line profiles parameterized by their velocity dispersion parameter b , cloud component velocity V_{lsr} and cloud column density N_{NaI} , were convolved with a Gaussian instrumental profile of 5.3 km s^{-1} width and fitted to the observed data. Inspection of the calibration lamp spectra supports our assumption of a Gaussian instrumental profile since no asymmetric tails are observed in the thorium lines. Both the D_2 and D_1 lines were fitted simultaneously, with the fewest components that seemed reasonable. Inflections in line shape, as a result of additional components in the wings of the stronger lines, often indicated whether another component should be added to the model. The hyperfine structure splitting of $\sim 1 \text{ km s}^{-1}$ of the individual D lines were not included in the adjustments since the resolution of the data is sufficiently broad to be affected by the splitting.

In most cases the assigned initial values of b were from 2.0 to 4.0 km s^{-1} to all components, but larger values are sometimes required, e.g. SAO 239531. Also the three free parameters (N_{NaI} , V_{lsr} , b) for each component were allowed to vary in an iterative nonlinear least-squares fit to the observed profile. Some parameters occasionally were held fixed at “reasonable” values in order to facilitate convergence of the fits, but are thought to be as well determined as those allowed to vary.

The average of the D_2 and D_1 best fit values of these parameters are listed in Table 2. A total of 125 entries are given. Each successive column gives the star’s name, component number, LSR radial velocity V_{lsr} , heliocentric radial velocity V_{\odot} , logarithm of the column density $\log N_{\text{NaI}}$, velocity dispersion b and the equivalent widths W_{D_2} and W_{D_1} , respectively.

The distribution of the absolute mean errors for $\log N_{\text{NaI}}$, V_{lsr} and b are shown in Figs. 5a-c. For narrow, isolated lines of moderate strength such errors are typically 1%-10% for $\log N_{\text{NaI}}$ and few hundredths of a km s^{-1} for b and V_{lsr} . For stronger, wider and more blended lines the uncertainties in $\log N_{\text{NaI}}$ are typi-

cally 5%-20%, and $0.1\text{-}0.4 \text{ km s}^{-1}$ in b and V_{lsr} . For the strongest saturated lines, uncertainties in the actual component structure are likely to be the dominant error source.

The theoretical uncertainty in the placement of the continuum level is approximately equal to the rms scatter divided by the square root of the number of points used to define it (Howarth & Phillips 1986). The statistical error on line flux values are given by $\sigma_F = \frac{\Delta\lambda\sqrt{n}}{S/N}$, where n is the number of observed data points in the absorption profile, $\Delta\lambda$ is the resolution element in $\text{\AA}/\text{pixel}$, and S/N is the signal-to-noise ratio of the exposure (Welsh et al. 1990). In most cases the continua are very well defined and statistical errors probably dominate the equivalent width errors. Typically for our observations, $n = 16$, $\Delta\lambda = 0.027\text{\AA}/\text{pix}$ and $S/N \geq 150$, so that $\sigma_F \leq 1 \text{ m}\text{\AA}$.

The star ι Lup has been previously observed at similar resolution (4 km s^{-1}) by Welsh et al. (1994). The parameters for ($\log N_{\text{NaI}}$, V_{lsr} , b) are (10.9 ± 0.02 , -13.8 ± 0.3 , 4.6 ± 0.3), and those obtained in this work are (11.0 ± 0.3 , -13.42 ± 0.09 , 4.3 ± 0.7). The remarkable agreement between the values is rather encouraging. Additional absorption features occur in some of the spectra of low $v \sin i$ stars shown in Fig. 4. The stellar Na I D lines are expected to be very weak throughout the class of B stars (being $\leq 2 \text{ m}\text{\AA}$ for stars earlier than B7), but the cases where stellar lines have been identified were removed from the multicomponent fit.

5 THE KINEMATICAL STRUCTURE

Histograms of the individual distributions of $\log N_{\text{NaI}}$, V_{lsr} and b are given in Figs. 5d to 5f. Inspection of Fig. 5d shows a clear division of the column densities around $\log N_{\text{NaI}} \approx 12.0 \text{ cm}^{-2}$. The average column density of the sub-samples is 11.2 cm^{-2} and 12.7 cm^{-2} , respectively, both with small dispersion of $\pm 0.6 \text{ cm}^{-2}$. Figure 5e shows that the distribution of the LSR velocities, although centered around 0 km s^{-1} , is skewed to the negative side. The velocity dispersion parameter b shows a concentration around 2.5 km s^{-1} and barely suggests another around 5.5 km s^{-1} . These trends are somewhat confirmed by Figs. 5g-i, that shows the plots of b vs. $\log N_{\text{NaI}}$, $\log N_{\text{NaI}}$ vs. V_{lsr} and V_{lsr} vs. b , respectively. For the sake of clarity few points of very high negative and positive LSR velocities have been excluded from these plots.

As one can see the lower column densities span the whole velocity dispersion range, and are concentrated mostly on the negative velocity range. On the other hand, the higher column densities are concentrated around $b \approx 3 \text{ km s}^{-1}$, and have velocities spread by $\pm 3 \text{ km s}^{-1}$ around zero km s^{-1} in the LSR frame. The apparent lack of points with $\log N_{\text{NaI}} \leq 10.5 \text{ cm}^{-2}$ for all b may be due to our detection limits. The lack of points with $b \leq 1.5 \text{ km s}^{-1}$ for $\log N_{\text{NaI}} \geq 11.5 \text{ cm}^{-2}$ may be due to our inability to resolve closely blended components.

5.1 Distribution of the interstellar gas components

To investigate the distribution and kinematics of the interstellar gas components along the line-of-sight plots of $\log N_{\text{NaI}}$, V_{lsr} and b as a function of the stellar distance are given in Fig. 6. The *left* column shows those stars with line-of-sight *inside* the clouds’ contours; the *middle* column those in their *outskirts*; and the *right* column those towards the *sheet*.

The plotting symbols indicate a further division of the components according to the line profile characteristics. The line profiles with a *single weak* feature are represented by the open triangles,

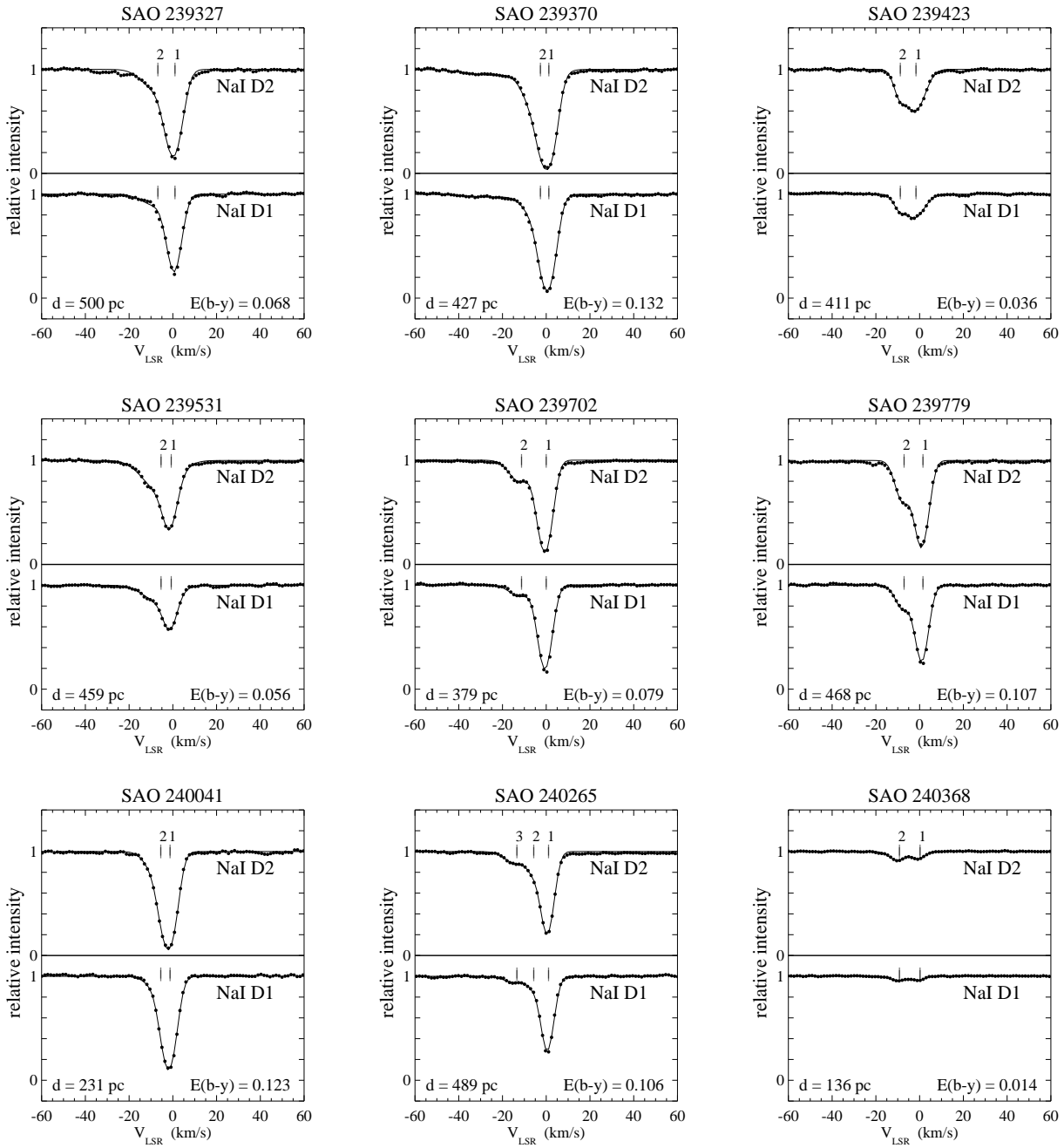


Figure 4. The observed Na I D absorption lines. The observed intensities are plotted as dots; the smooth curves are theoretical line profiles with the parameters given in Table 3. The tick marks and the corresponding number identifies the fitted components. The zero point of the velocity scale is referred to the rest wavelength of the D₂ and D₁ lines

while those profiles with a *single strong* feature are represented by the solid triangles. The profiles with *two weak* features are represented by the plusses and asterisks, which indicate the features with velocity similar to the single weak and single strong components, respectively. The profiles with *two or more* features are represented by the squares and circles. The open and solid squares indicate those features similar to the single weak and to the single strong components. The open circles indicate the other components, i.e., the third, fourth and so on.

The structure of the column density *vs.* distance diagrams for the stars *inside* the clouds' contours, in their *outskirts* and towards

the *sheet* is fairly similar. *Single weak* components are seen for the stars closer than 60–80 pc from Sun (open triangles and plusses), and for most of the more distant stars along the distance range (open squares). On the other hand, the *single strong* component is seen only for stars more distant than 120–150 pc from the Sun (solid triangles, asterisks and solid squares). The open circles tend to appear at distances greater than 300–350 pc, but without clear correlation with the column densities or the radial velocities.

The velocities of the components identified along the line of sight also have a similar structure for the stars *inside* the clouds' contours, in their *outskirts* and towards the *sheet*. The *single weak*

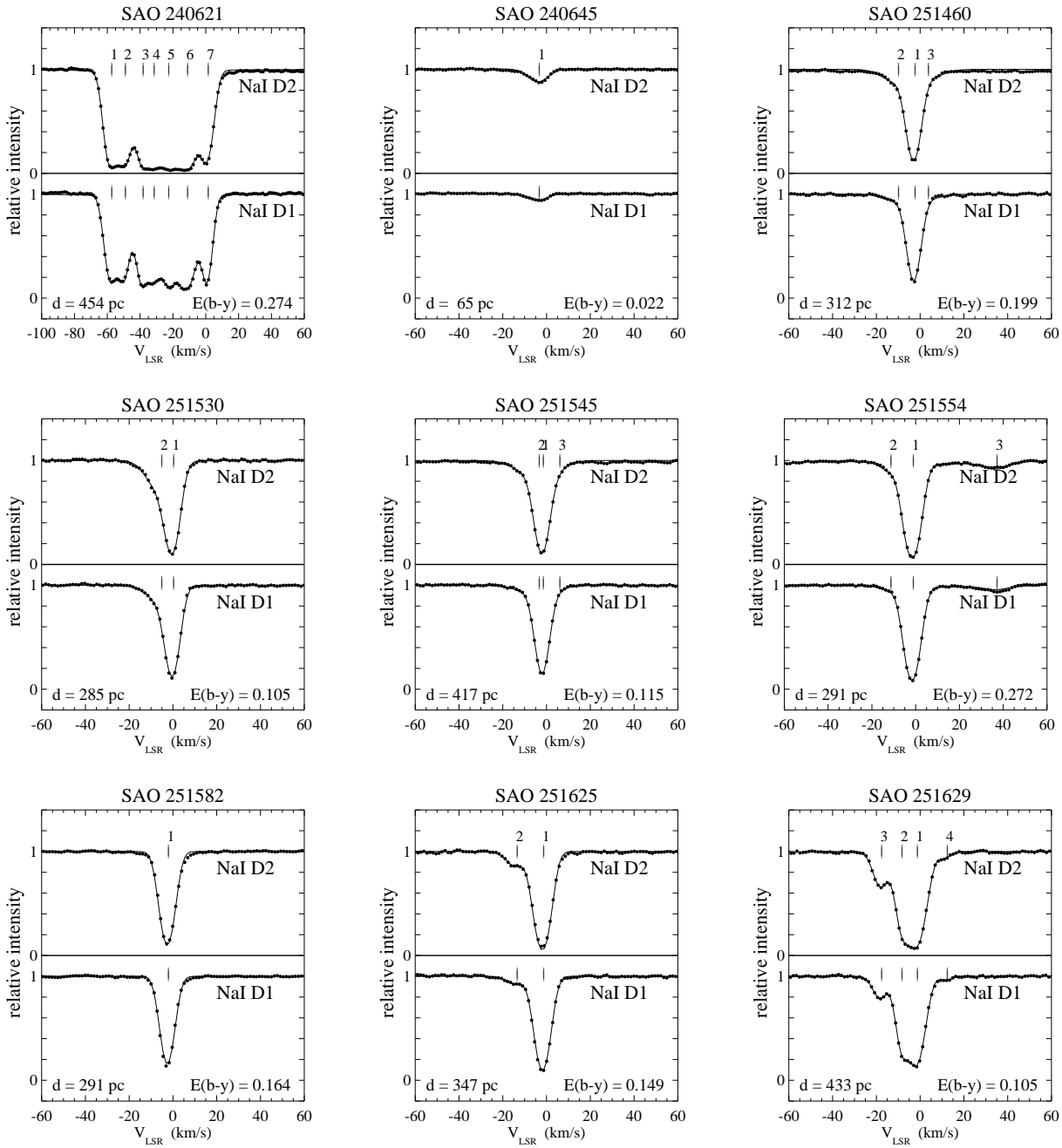


Figure 4. (Continued)

component (open triangles, open squares and plusses) has velocity more negative than -5 km s^{-1} , while the *single strong* component (solid triangle, solid square and asterisks) is centered at 0 km s^{-1} in the LSR frame. The fact that the plusses and asterisks show kinematic structure consistent with those of the *single weak* and the *single strong* components, respectively, suggests that the material have some inhomogeneities. The open circles appear in the whole range of radial velocities.

The velocity dispersions of the components also have a similar structure for the stars *inside* the clouds' contours, in their *outsirts* and towards the *sheet*. The *single weak* component has $b \approx 5.5 \text{ km s}^{-1}$. On the other side the *single strong* component has $b \approx 2.5 \text{ km s}^{-1}$.

The b value is a measure of both thermal and turbulent velocities in an interstellar cloud. We have $b = \sqrt{\frac{2kT}{m} + 2v_t^2}$, where v_t is the rms turbulent velocity, k is the Boltzmann's constant, T is the kinetic temperature and m is the mass of the atom. There is no independent way to determine the degree of turbulence within the material, but some qualitative considerations can be done. The typical kinetic temperature of interstellar diffuse clouds is generally taken to be about $80 - 115 \text{ K}$, from observations of rotational excitation of H_2 (Savage et al. 1977). For NaI this corresponds to $0.24 \leq b \leq 0.29 \text{ km s}^{-1}$. In this case the upper limits to v_t for the *weak* and *strong* components would be 1.8 and 3.9 km s^{-1} . Assuming a sound speed for diffuse interstellar clouds about 0.7 km s^{-1} (Spitzer 1978) the observed components are either signifi-

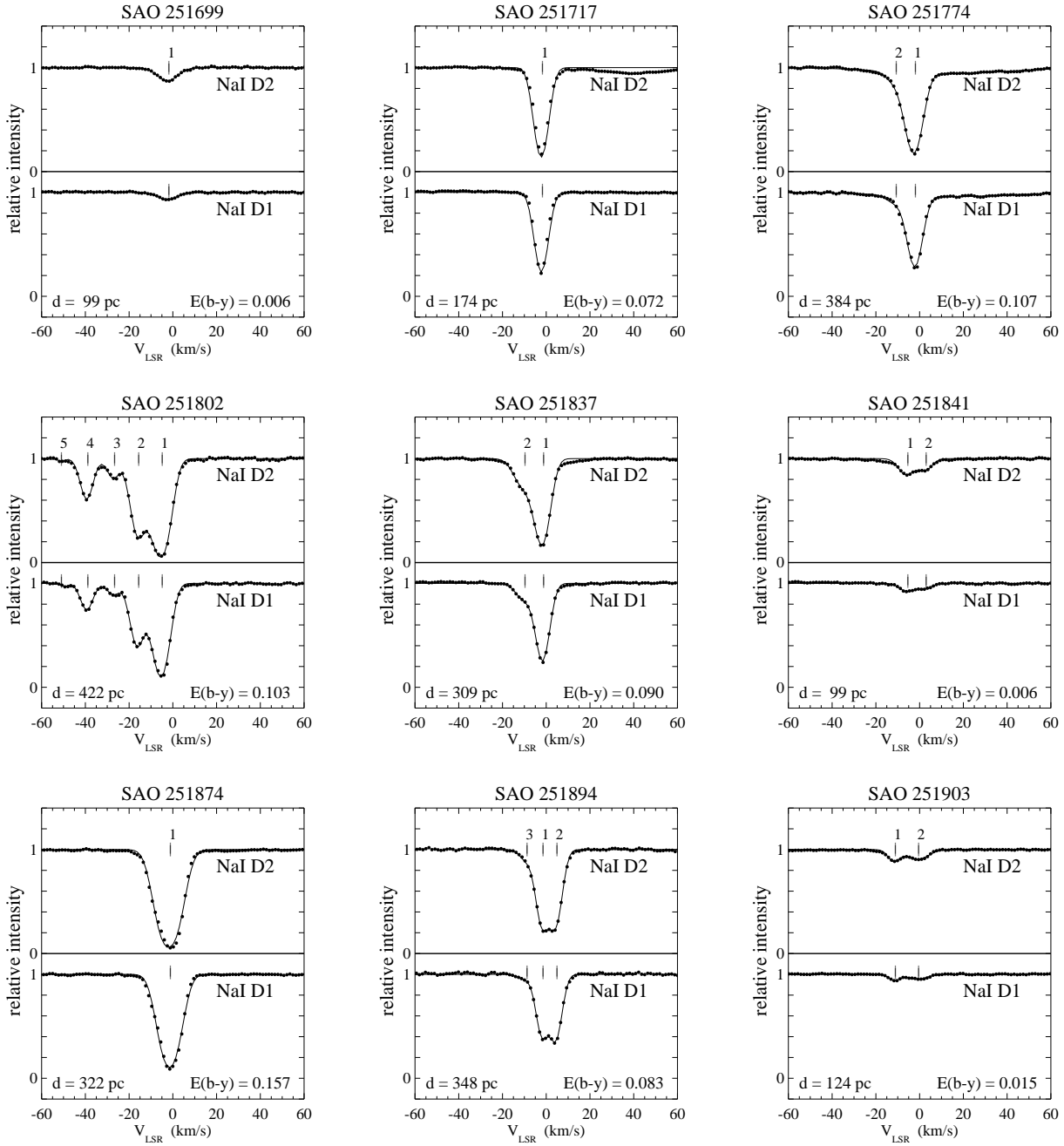


Figure 4. (Continued)

cantly hotter than a standard diffuse cloud or are subject to supersonic turbulent motions.

5.2 The gas sheet-like features

To look for a possible association of the interstellar gas components with the observed dust features in this direction, $\log N_{\text{Na I}}$, V_{LSR} and b as a function of the $E(b-y)$ colour excess have been plotted in Fig. 7. The columns and symbols have the same meaning as for Fig. 6. It can be seen that the *strong* component is only picked up by the reddened stars, i.e., those with $E(b-y) \geq 0^{\text{m}}050$, whereas the *weak* component is picked up by both reddened and unreddened

stars, suggesting that dust and gas apparently have the same distribution along the line of sight.

The average column density of the *weak* component ($\log N_{\text{Na I}} \sim 11.2 \text{ cm}^{-2}$), would correspond to $N_{\text{H}} \sim 3 \times 10^{19} \text{ cm}^{-2}$. It is worth noticing at this point that, in Fig. 6a of Paper I, around 60-70 pc the dispersion of the $E(b-y)$ increases, with the lower limit becoming slightly shifted to positive values. This indicates that the spectroscopy has provided a finer tuning of the existing low column density components, more difficult to disentangle based only on the colour excess values. On the other hand, it shows that the observed increase in the dispersion of $E(b-y)$ is real, and not due to observational errors, attesting the high quality of the photometric data and method.

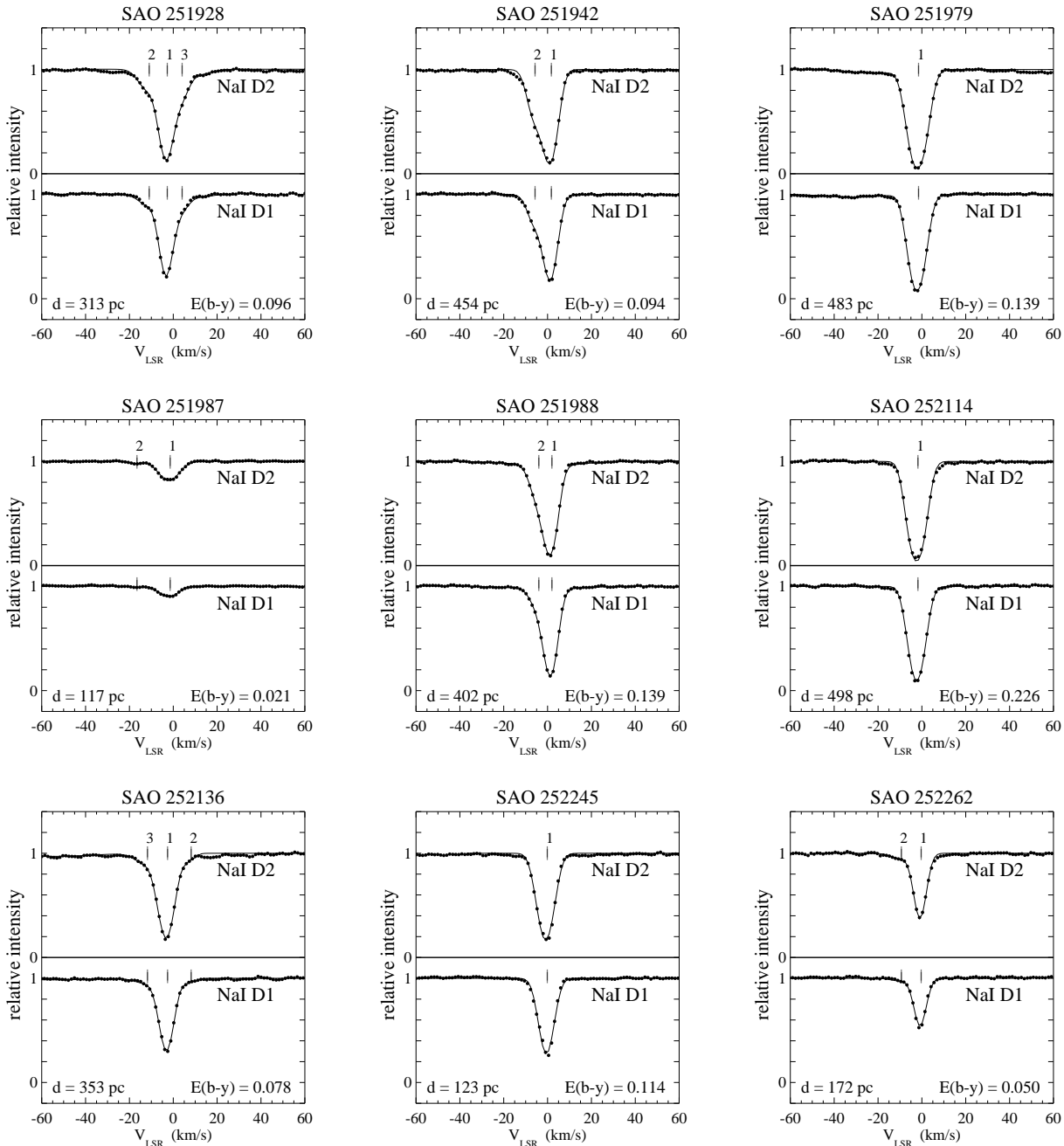


Figure 4. (Continued)

There appears to be a common envelope of minimum and maximum column density, centered in a narrow distance slot around 120-150 pc, that remain unchanged up to 350-400 pc, suggesting that a second volume of low density may have been reached. The complete range of column densities from $\log N_{\text{NaI}} \sim 10.7$ to 11.7, is also shown by the stars centered around 60 pc, suggesting a sheet-like structure.

Interestingly, the minimum and maximum column densities of the *strong* component ($\log N_{\text{NaI}} = 12.3$ and 13.2 cm^{-2}) correspond to $E(b-y) \sim 0^{\text{m}}050$ and $0^{\text{m}}300$, respectively, if it is assumed that the standard relationship between $\log N_{\text{NaI}}$ and $\log N_{\text{H}}$ (Ferlet et al. 1985) and $E(b-y)$ and $\log N_{\text{H}}$ (Knude 1978) are valid. This may suggest that the high column densities may be the

gas related to the dust sheet-like structure, reported in Paper I. Since the Coalsack, Musca and Chamaeleon are also located around 150 ± 30 pc they seem also to be part of the gas composing the sheet.

Assuming that the observed stars are within different dark clouds the column densities, radial velocities and velocity dispersions, shown in Figs. 4 to 6, could be either the effect of a common structure containing the embedded molecular clouds or just an effect of different superposing structures. In order to investigate how the parameters ($\log N_{\text{NaI}}$, V_{lsr} , b) are distributed over the studied area we have used the eight sub-areas delineated by the horizontal and vertical dashed lines and identified by the roman numbers in Fig. 2.

Figures 8a and b show the distribution of $\log N_{\text{NaI}}$ (*left*),

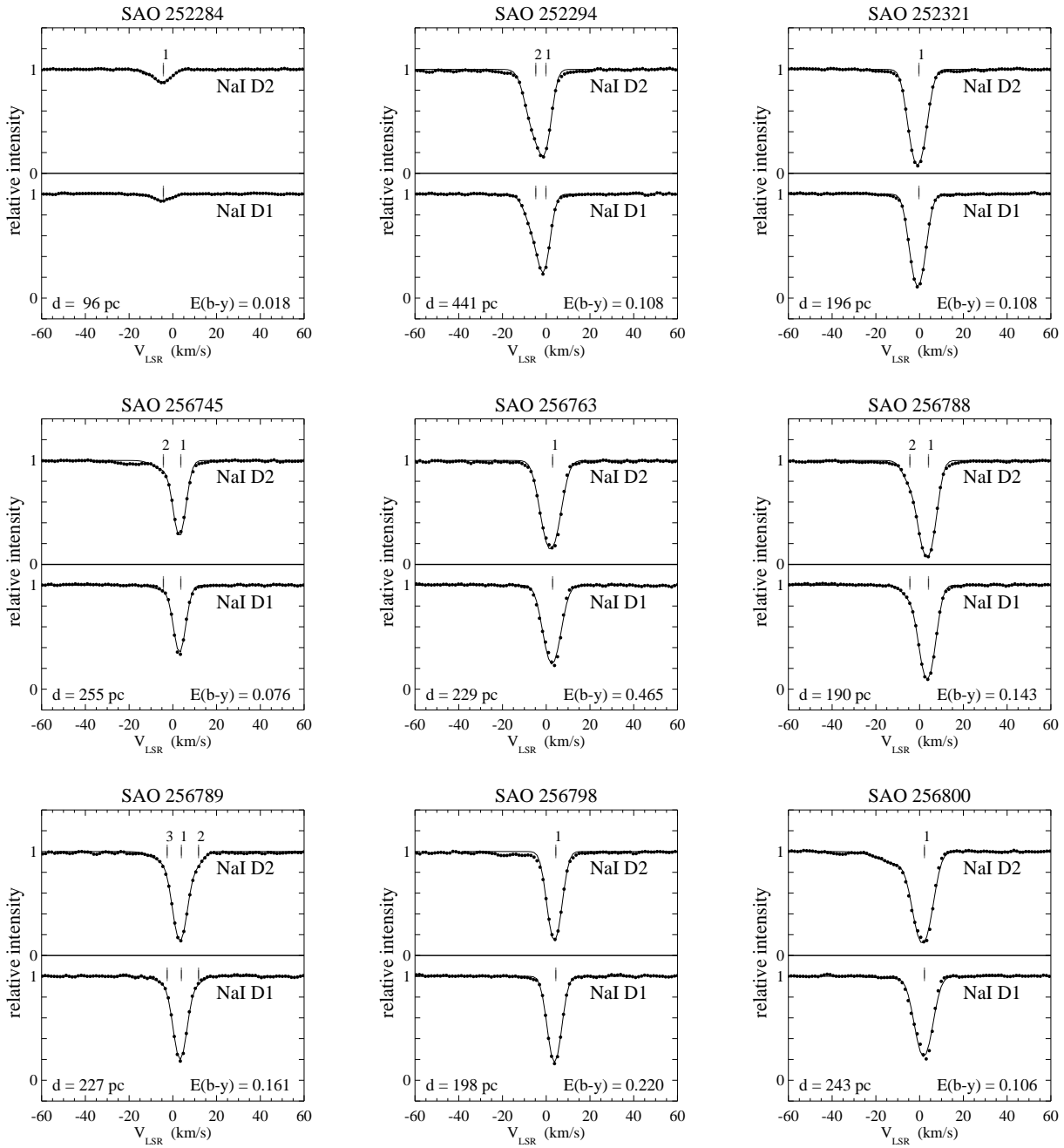


Figure 4. (Continued)

V_{LSR} (middle) and b (right) against the Galactic longitude and latitude, respectively, for the eight sub-areas. The symbols have the same meaning as for Fig. 6, and the vertical and horizontal dashed lines indicate the division between the sub-areas. The *strong* and *weak* components are present – and well separated – everywhere. The gas components form two extended interstellar features, that cover the whole connecting area.

Note, however, that the radial velocity of the *strong* component seems to increase from -3 km s^{-1} near the galactic plane to $+3 \text{ km s}^{-1}$ near the southern parts. This trend would be expected from an expanding bubble with the center around $l \approx 309^\circ$, $b = -9^\circ$. This fact is quite interesting given the fact that high thermal pressure has been measured for the hot gas phase for a nearby

direction ($l = 309^\circ$, $b = -15^\circ$) from a combination of ROSAT 0.25 keV and optical data (Knude et al. – in preparation).

6 DISCUSSION

The analysis of the identified components indicates that the interstellar gas is distributed in two extended sheet-like structures permeating the whole area, one at $d \leq 60 \text{ pc}$ and another around 150 pc from the Sun. The nearby feature is approaching the Sun with average radial velocity of -7 km s^{-1} , has low average column density ($\log N_{\text{Na I}} \approx 11.2 \text{ cm}^{-2}$) and is either hotter or more turbulent than the *strong* component, with velocity dispersion $b \approx$

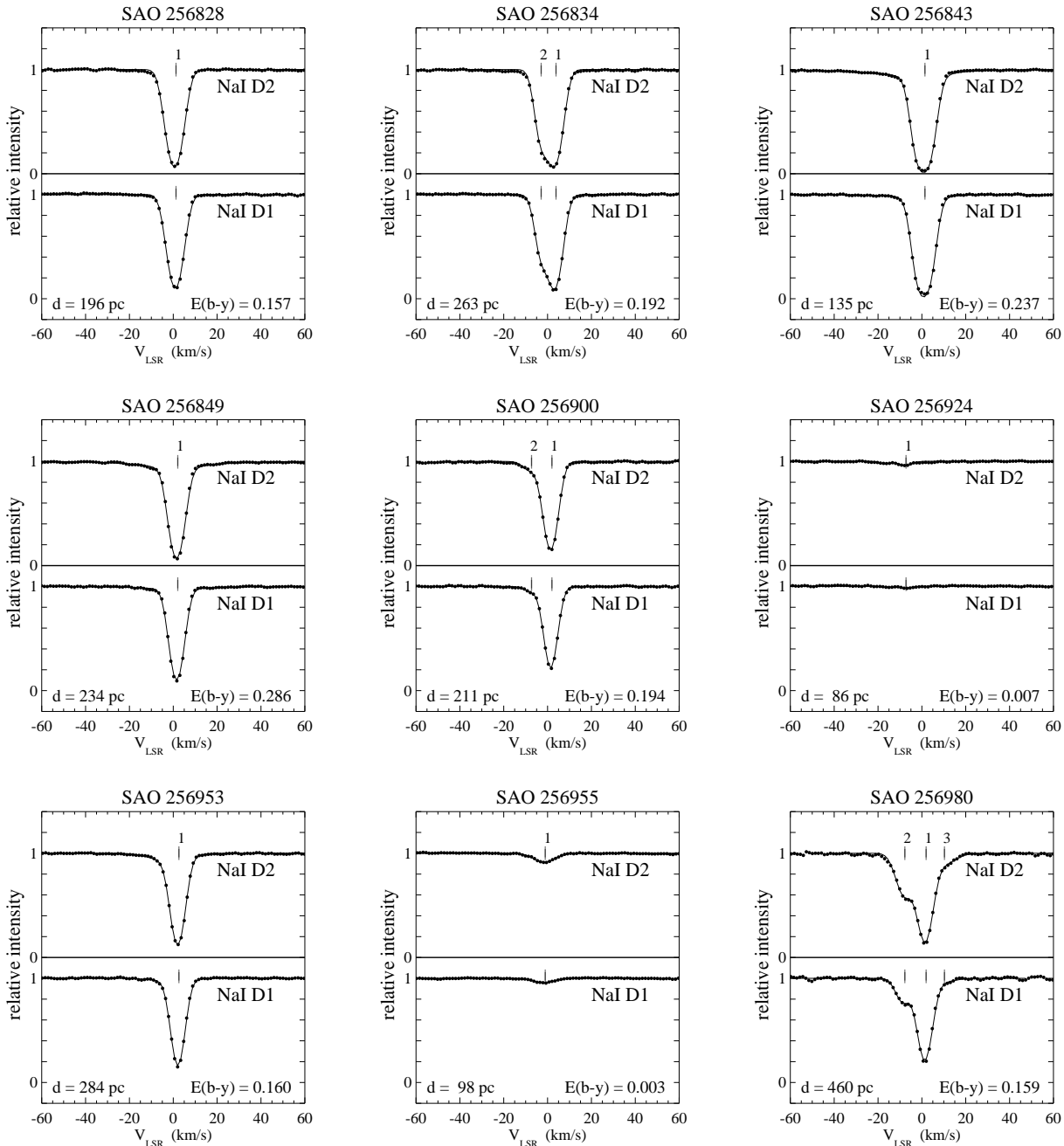


Figure 4. (Continued)

5 km s^{-1} . The more distant feature has column densities between $12.3 \leq \log N_{\text{Na I}} \leq 13.2$, average velocity dispersion $b \approx 2.5 \text{ km s}^{-1}$ and seems associated to the dust sheet observed towards the Coalsack, Musca and Chamaeleon direction. Its velocity is centered around 0 km s^{-1} , but there is a trend for increasing from -3 km s^{-1} near $b = 1^\circ$ to 3 km s^{-1} near $b = -18^\circ$.

There seems to be a common envelope of minimum and maximum column density, centered in a narrow distance slot around $120 - 150 \text{ pc}$, that remains unchanged up to 350 pc , suggesting that a volume of low density may have been reached. After that, a third group of high negative and positive velocity components seemingly arise around $300\text{-}350 \text{ pc}$ from the Sun, however, without indications of an extended structure.

6.1 The nearby, low column density feature

Details of the overall distribution of the ISM ($d \leq 500 \text{ pc}$) along the studied direction have been extensively discussed in Paper I. The kinematics of the nearby gas has been reviewed by Frisch & York (1986). Details of the velocity structure in the region ($360^\circ \leq l \leq 295^\circ$ and $0^\circ \leq b \leq 30^\circ$), encompassing most of the Sco-Cen association, have been discussed by Crawford (1991).

In the immediate solar neighbourhood the observational data suggest that the Sun is located within but close to the edge of the Local Interstellar Cloud (LIC). First identified from its kinematics by Lallement & Bertin (1992), the LIC was modelled by Redfield & Linsky (2000) as roughly spherical with dimensions of

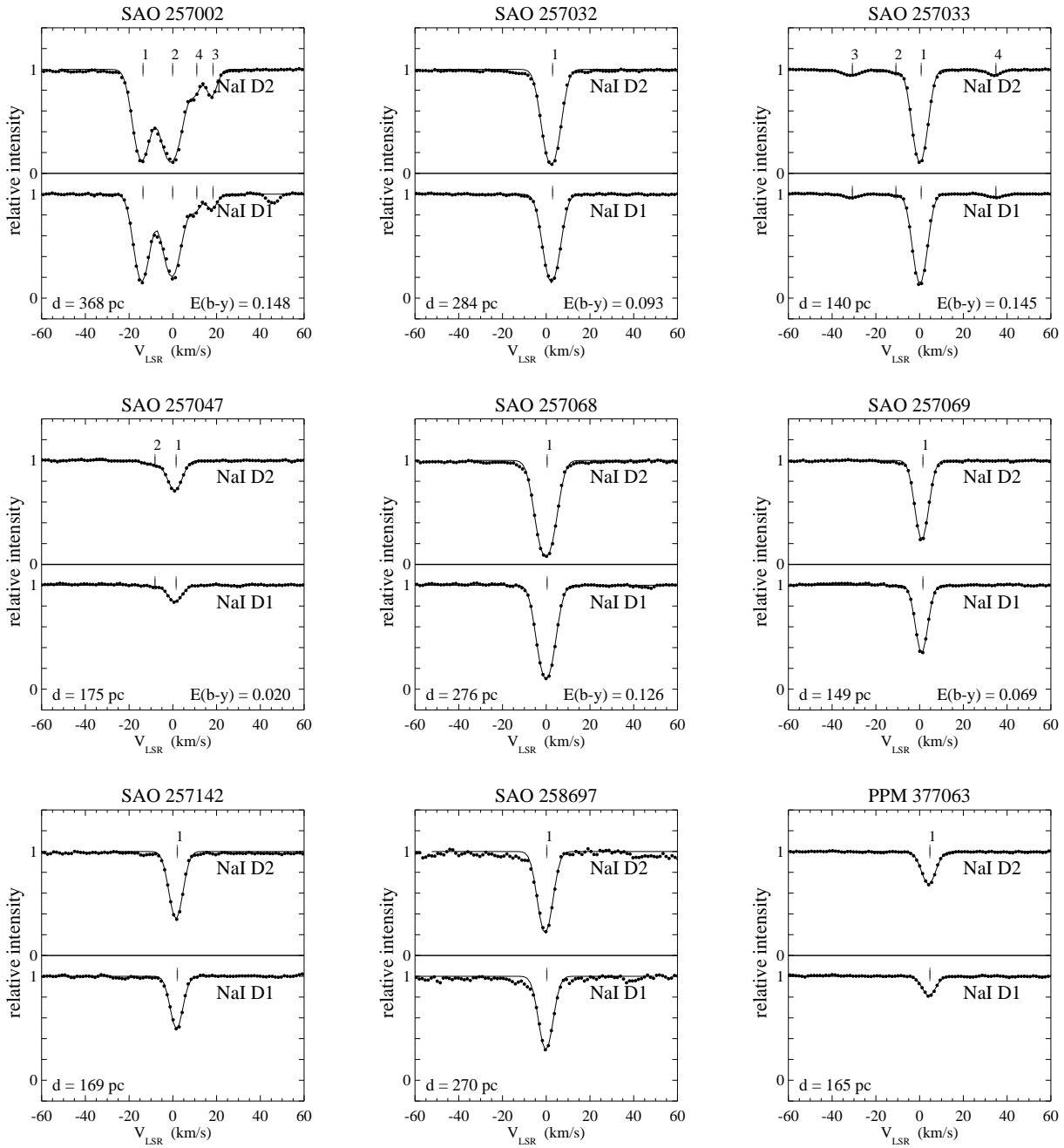


Figure 4. (Continued)

5–8 pc, warm ($T \approx 7000$ K), low density ($n_{\text{HI}} < 0.1 \text{ cm}^{-3}$) and mostly neutral ($n_e/n_{\text{HI}} < 0.5$). Its largest column density is about $2 \times 10^{18} \text{ cm}^{-2}$ towards $l = 157^\circ$, $b = -25^\circ$.

Moving at a heliocentric velocity of $\approx 26 \text{ km s}^{-1}$ towards $l \approx 186^\circ$, $b \approx -16^\circ$ (cf. Lallement et al. 1995; Lallement 1998), the LIC flows through the solar system and resonantly scatters solar H I (Lyman α) and He I ($\lambda 584$) radiation. This flow, is referred to as the local interstellar wind (LISW).

The LIC and other warm clouds with similar temperatures but a wide range of metal depletions, are embedded in an irregularly shaped region, whose radius ranges from 30 to 300 pc, and is deficient in dense neutral hydrogen compared to the galactic average (e.g. Frisch & York 1983; Paresce 1984; Snowden et al. 1990;

Tinbergen 1982; Warwick et al. 1993; Welsh et al. 1994). Usually called Local Bubble, this cavity is thought to contain hot ($T \approx 10^6$ K), low-density ($n_{\text{HI}} \leq 0.025 \text{ cm}^{-3}$) gas and as recently shown by the ROSAT and EUVE shadowing experiments, coexists with the neutral atomic and molecular gas within its interior (e.g. Bowyer et al. 1995; Kerp et al. 1993; Snowden et al. 1991, 1995, 1998; Wang & Yu 1995). It is, however, worth noticing that Cravens (2000) has recently shown that heliospheric X-ray emission can account for about 25%-50% of the observed soft X-ray background intensities, which may put in doubt if the Local Bubble really contains the million degree hot gas.

Optical interstellar absorption line studies within 100 pc of the Sun show evidence of a flow of material analogous to the LISW.

Table 2. Profile fit results for the Na I D absorption-lines. Each successive column gives the star's name, component number, LSR radial velocity V_{lsr} , column density ($\log N_{\text{NaI}}$), velocity dispersion b and the equivalent width of the D₂ and D₁ lines

Star	C	V_{LSR}	V_{\odot}	$\log N_{\text{NaI}}$	b	WD ₂	WD ₁	Star	C	V_{LSR}	V_{\odot}	$\log N_{\text{NaI}}$	b	WD ₂	WD ₁
		km s ⁻¹	km s ⁻¹	cm ⁻²	km s ⁻¹	mÅ	km s ⁻¹			mÅ	km s ⁻¹	cm ⁻²	km s ⁻¹	mÅ	
239327	1	0.5	10.0	12.3	3.2	162.9	122.4	251928	1	3.5	11.4	11.5	3.5	48.5	26.2
	2	-7.4	2.0	11.5	8.0	60.6	34.5		2	-3.3	4.6	12.6	2.1	139.5	118.9
239370	1	0.6	9.8	13.0	2.5	188.2	168.9		3	-11.5	-3.5	11.4	4.8	41.7	21.9
	2	-3.2	6.0	11.9	7.1	137.1	76.7	251942	1	1.2	8.9	12.6	2.4	157.9	134.6
239423	1	-2.2	6.8	11.7	5.0	88.5	48.8		2	-6.2	1.5	11.7	2.7	68.3	39.8
	2	-9.4	-0.4	11.2	1.4	27.0	14.8	251979	1	-2.1	5.5	12.7	3.4	215.4	188.5
239531	1	-1.3	7.5	11.8	2.7	89.5	52.3	251987	1	-2.0	6.1	11.4	5.4	43.0	21.7
	2	-5.9	3.0	11.8	9.5	108.5	56.9		2	-17.0	-8.9	10.2	0.3	3.3	1.2
239702	1	-0.5	7.9	12.6	2.4	154.5	132.0	251988	1	1.4	9.9	13.9	1.4	150.1	138.3
	2	-11.8	-3.4	11.4	5.9	50.5	26.5		2	-4.5	3.9	11.5	3.3	56.2	30.5
239779	1	1.0	9.2	12.5	2.2	133.9	111.0	252114	1	-2.4	4.8	12.8	3.1	205.3	176.4
	2	-7.7	0.5	11.6	3.2	65.8	37.1	252136	1	7.7	15.0	10.9	0.2	9.3	6.2
240041	1	-1.9	5.7	12.9	2.4	176.4	156.5		2	-3.1	4.3	12.3	3.1	152.2	115.4
	2	-6.0	1.6	11.6	6.2	67.4	35.8		3	-12.3	-5.0	11.1	5.8	23.8	11.5
240265	1	0.5	7.5	12.5	1.9	121.4	105.2	252245	1	-0.7	6.6	12.3	3.2	162.6	125.1
	2	-6.3	0.7	11.0	1.5	19.3	10.4	252262	1	-0.8	6.2	12.0	1.9	88.7	62.7
	3	-13.9	-7.0	11.2	6.0	29.1	14.9		2	-9.9	-2.8	10.7	4.7	10.3	5.2
240368	1	-0.4	6.3	10.7	1.9	10.1	5.0	252284	1	-4.9	1.0	11.1	4.7	26.1	12.3
	2	-9.7	-3.1	10.9	4.3	16.1	8.4	252294	1	-0.6	6.3	12.5	1.6	101.2	95.1
240621	1	0.8	6.9	12.6	2.9	178.5	133.9		2	-5.3	1.6	11.9	4.0	113.8	65.9
	2	-11.8	-5.6	12.7	5.9	312.8	269.5	252321	1	-0.9	6.3	12.8	2.7	182.2	156.9
	3	-23.3	-17.2	12.6	5.3	274.4	225.2	256745	1	3.1	14.0	12.4	1.6	103.5	88.4
	4	-32.2	-26.0	12.3	2.3	134.3	102.4		2	-4.9	6.0	10.9	5.0	16.8	8.5
	5	-38.8	-32.7	15.3	0.5	277.4	223.2	256763	1	2.3	13.3	12.4	3.9	186.5	148.7
	6	-49.6	-43.5	12.5	2.6	160.7	131.7	256788	1	3.5	14.4	12.9	2.6	179.0	165.9
	7	-58.1	-52.0	12.6	3.0	188.9	149.6		2	-4.9	6.0	11.2	2.7	29.8	15.1
240645	1	-3.8	2.3	11.2	5.1	28.0	13.4	256789	1	11.2	22.0	10.9	2.1	16.5	8.6
251460	2	-2.9	7.1	13.0	1.8	144.6	130.6		2	3.4	14.2	12.7	2.0	138.7	122.0
	3	-10.4	-0.4	11.3	8.2	38.8	19.9		3	-3.2	7.7	11.2	6.5	27.3	13.9
	1	3.3	13.3	11.2	8.6	27.6	14.0	256798	1	3.8	14.5	12.8	2.0	141.3	131.1
251530	1	-0.3	9.4	13.0	2.0	152.4	145.2	256800	1	1.7	12.5	12.4	3.9	189.1	153.8
	2	-5.6	4.1	11.7	7.3	86.4	47.8	256828	1	0.8	11.3	12.7	3.0	191.6	171.6
251545	1	-2.0	7.7	14.9	1.1	214.4	167.8	256834	1	3.4	13.8	12.9	2.4	168.2	157.9
	2	-13.2	-3.5	10.1	0.2	2.8	0.8		2	-3.5	7.0	12.1	1.5	80.6	66.8
251554	1	36.7	46.5	11.0	6.9	17.7	9.0	256843	1	0.8	11.2	14.6	2.1	258.6	235.9
	2	-1.6	8.2	12.9	2.7	190.6	174.7	256849	1	1.6	11.8	14.2	1.6	182.4	156.5
	3	-11.8	-2.0	10.9	4.3	16.1	8.2	256900	1	1.4	11.0	12.6	2.2	144.2	120.6
251582	1	-2.6	7.0	12.7	2.3	161.1	140.5		2	-7.8	1.7	10.9	2.8	13.4	7.3
251625	1	-1.8	7.6	12.9	2.6	188.4	166.8	256924	1	-7.7	1.9	10.5	2.4	6.1	2.6
	2	-14.0	-4.5	11.2	4.8	29.9	15.4	256953	1	2.1	11.4	13.1	1.8	145.3	131.9
251629	1	11.8	21.0	10.9	0.3	9.1	4.9	256955	1	-1.6	7.3	11.0	5.7	20.4	10.0
	2	-1.8	7.4	12.5	3.7	213.2	162.9	256980	1	9.8	18.2	11.1	6.5	27.6	9.0
	3	-8.8	0.4	12.6	1.2	83.4	86.7		2	1.4	9.9	12.4	2.7	147.1	133.0
	4	-18.1	-8.9	11.6	3.2	59.1	34.0		3	-8.2	0.2	11.7	3.5	77.8	36.9
251699	1	-2.4	7.0	11.2	5.4	29.2	15.0	257002	1	17.8	26.1	11.4	0.8	31.6	16.9
251717	1	-2.2	6.7	12.5	2.3	145.4	121.1		2	10.4	18.7	11.4	0.6	24.3	18.3
251774	1	-2.4	6.2	12.3	3.4	162.5	122.4		3	-0.6	7.7	12.5	4.4	223.1	169.4
	2	-11.2	-2.6	11.1	4.0	20.1	14.4		4	-14.2	-5.9	12.5	3.1	170.1	150.4
251802	1	-5.4	4.2	12.7	3.5	212.2	178.6	257032	1	2.4	9.9	12.6	3.3	188.3	162.5
	2	-16.1	-6.5	12.2	2.9	128.7	98.6	257033	1	34.3	42.0	10.7	3.5	9.8	5.0
	3	-27.2	-17.6	11.2	2.1	26.0	15.0		2	0.2	7.9	13.1	1.9	155.7	141.1
	4	-39.4	-29.8	11.6	2.1	56.5	35.8		3	-11.4	-3.7	10.4	0.3	4.2	2.3
	5	-51.4	-41.8	10.4	0.2	2.6	3.1		4	-31.3	-23.6	10.8	5.1	12.4	6.3
251837	1	-1.7	6.5	12.4	2.7	149.8	117.7	257047	1	1.0	9.0	11.4	2.9	46.3	25.0
	2	-10.2	-2.0	11.5	4.3	56.7	28.5		2	-8.7	-0.6	10.6	5.2	9.0	2.8
251841	1	2.4	10.9	11.0	3.1	18.2	8.1	257068	1	-0.1	7.4	12.6	3.6	211.5	183.2
	2	-6.0	2.5	11.1	3.4	26.0	12.8	257069	1	1.0	9.0	12.3	1.9	116.3	90.6
251874	1	-1.6	7.1	12.6	5.3	281.9	232.4	257142	1	1.6	9.7	12.0	2.3	100.8	72.0
251894	1	4.4	13.2	12.3	1.8	103.7	86.6	258697	1	-0.3	8.4	12.3	2.7	132.7	114.5
	2	-2.0	6.8	12.5	1.4	98.7	74.7	377063	1	4.2	15.8	11.5	2.8	50.3	28.3
	3	-9.3	-0.5	10.9	2.6	14.1	7.6								
251903	1	-1.0	7.2	11.1	5.5	23.3	10.2								
	2	-11.6	-3.5	10.9	1.2	14.3	7.2								

Assuming that the Sun is embedded within a single coherently moving interstellar wind, from a direction (l_w, b_w) with velocity v_w , Crutcher (1982) obtained the following vector (l_w, b_w, v_w) = (345°, -10°, -15 km s⁻¹). In a similar analysis Frisch & York (1986) obtained (354°, +3°, -12 km s⁻¹) and Crawford (1991) obtained (301°, +59°, -9 km s⁻¹). A possible description for this flow assumes that the LISM is material which belongs to the surface of an expanding shell centered on the Sco-Cen association. Crawford

(1991) has obtained an expansion velocity of 7–9 km s⁻¹ assuming the center at ($l = 320^\circ, b = +10^\circ$), the distance to the Sun of 140 pc and the radius of 110 pc, as suggested by de Geus (1992).

Another possible explanation for the existence of the neutral clouds and their predominant flow away from the Sco-Cen association is a consequence of the interaction between the Local and Loop I Bubbles (see Sect. 6.2) and subsequent local fragmentation of the interaction zone (Breitschwerdt et al. 2000).

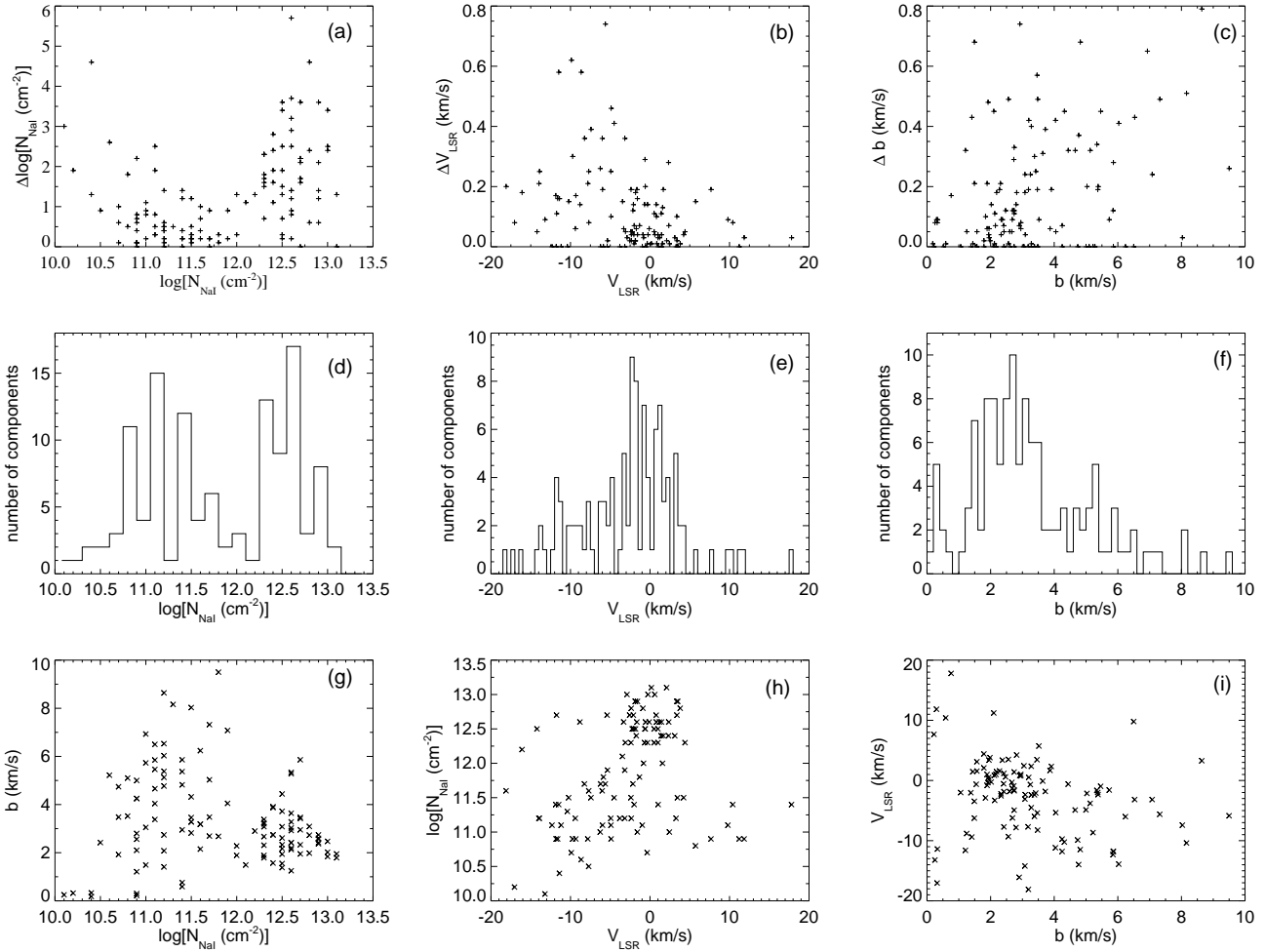


Figure 5. Distribution of the free parameters determined in the profile fits and their absolute mean errors. **a-c** Distribution of the absolute mean errors in the fitted values of $\log N_{\text{Na I}}$, V_{LSR} and b , respectively. For narrow, isolated lines of moderate strength such errors are typically 1%-10% for $\log N_{\text{Na I}}$ and few hundredths of a km s^{-1} for b and V_{LSR} . For stronger, wider and more blended lines the uncertainties in $\log N_{\text{Na I}}$ are typically 5%-20%, and $0.1\text{-}0.4 \text{ km s}^{-1}$ in b and V_{LSR} . **d-f** Histogram of $\log N_{\text{Na I}}$, V_{LSR} and b , respectively. There is a clear division of the column densities around $\log N_{\text{Na I}} \approx 12.0 \text{ cm}^{-2}$. The LSR velocities, although centered around 0 km s^{-1} , are skewed to the negative side. Also the velocity dispersion parameter b shows a concentration around 2.5 km s^{-1} and another around 5.5 km s^{-1} . **(g)** Distribution of $\log N_{\text{Na I}}$ vs. b . **(h)** Distribution of $\log N_{\text{Na I}}$ vs. V_{LSR} . **(i)** Distribution of V_{LSR} vs. b . The lower column densities span the whole velocity dispersion range, and are concentrated mostly on the negative velocity range. On the other hand, the higher column densities are concentrated around $b \approx 3 \text{ km s}^{-1}$, and are essentially at rest in the LSR frame; although a $\pm 2 \text{ km s}^{-1}$ spread may be present. For the sake of clarity few points of very high negative and positive LSR velocities have been excluded from these plots. Further details can be found in the text

Since the closest star in our sample is at 65 pc the LIC cannot be addressed properly, neither the distance of the lower column density component. However, according to Welsh et al. (1994, and references therein) the column densities of the nearby feature observed in this work should not be much closer than 50 pc from the Sun.

For the latitude/longitude region observed in our work the velocities predicted by the interstellar wind flow vector and the expanding shell models give essentially the same results (Crawford 1991, cf. his Fig. 3). In any case the velocity of the low column density component is consistent with the previous results, and indicate an outflow from the Sco-Cen association.

A more recent discussion by Cha et al. (2000) also using Na I D line data and *Hipparcos* distances proposes components at three distinct heliocentric velocities in the Puppis-Vela region. Their

component A with the velocity in the range from $+6$ to $+9 \text{ km s}^{-1}$ covers part of the region presently discussed.

From the distances of Table 1 and heliocentric velocities from Table 2 we construct Fig. 9 of V_{\odot} vs. distance and notice that Cha et al.'s component A is seen in two stars closer than 100 pc and in fact seems present in all stars all the way to 450 pc, this implies that component A covers all of our surveyed region, indeed a sheet nearer than about 100 pc. Two stars marginally have absorption features at component B's lower velocity limit (12 km s^{-1}), these stars are at 100 pc and 130 pc respectively. Otherwise component B is seen in most stars beyond 180 pc; the upper distance limit is very sharply defined by component B's upper limit at 15 km s^{-1} . No stars beyond ≈ 350 pc shows any indication of component B. Component C ($21 - 23 \text{ km s}^{-1}$) is virtually absent from our region and is only observed for galactic longitude less than 275° in Cha et al.'s survey, far from our region. Four stars closer than 100 pc show ab-

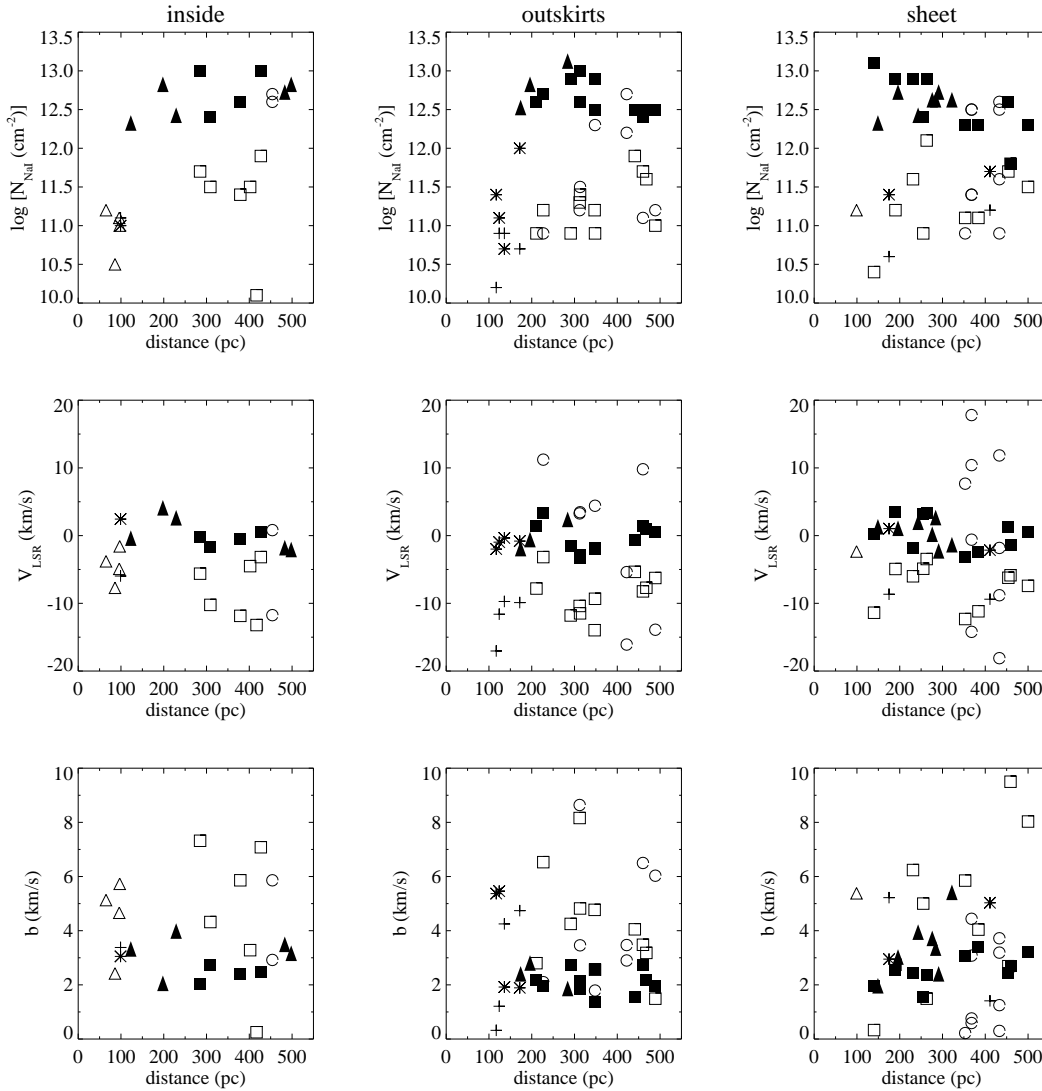


Figure 6. Plots of $\log N_{\text{NaI}}$, V_{LSR} and b against the stellar distances. From left to right the columns show the stars with line-of-sight *inside* the clouds' contours, in their *outskirts*, and towards the *sheet*. The line profiles with a *single weak* feature are represented by the open triangles, while the profiles with a *single strong* feature are represented by the solid triangles. The profiles with *two weak* features are represented by the pluses and crosses, which indicate the features with velocity similar to the single weak and strong components, respectively. The profiles with *two or more* features are represented by the squares and circles. The open and solid squares indicate those features similar to the single weak and strong components. The open circles indicate the other ones, i.e., the third, fourth, etc. The same structure for the *weak* and the *strong* components suggests one interstellar gas at $d \leq 60$ pc and other ≈ 120 – 150 pc. The *strong* component ($\log N_{\text{NaI}} \approx 12.7$ cm^{-2}) is spread ± 3 km s^{-1} around the zero velocities, and has low velocity dispersion $b \approx 2.5$ km s^{-1} . The *weak* component ($\log N_{\text{NaI}} \approx 11.2$ cm^{-2}) is approaching the Sun with average V_{LSR} around -7 km s^{-1} and have larger velocity dispersion $b = 5$ km s^{-1} . Further details in the text

sorption in a narrow interval from $+1$ to $+4$ km s^{-1} , this interval is hardly represented between 100 and 400 pc from where it is again present in almost any star. A fifth group of absorption has velocities between -2 and -4 km s^{-1} for three stars between 120 and 140 pc, lines in this interval disappear for larger distances but reappear between 300 and 400 pc. Locally, that is for distances less than 150 pc, we confirm three interstellar kinematic groups with absorption lines in the intervals: $[-5,0]$, $[0,5]$ and $[5,10]$ the second of which represents the volume within 100 pc whereas the other two both are present between 120 and 150 pc. The local ISM thus seems more complicated than proposed in Cha et al. (2000) investigation. One could speculate whether the interval $[0,5]$ is representing the

local undisturbed material and $[5,10]$ and $[-5,0]$ the expansion of the Local and the Sco–Cen Bubbles respectively?

Fig. 9 also indicates that the distribution of heliocentric velocities for the diffuse components changes character between 300 and 350 pc. Closer than 300 pc there is a set of velocities exceeding 10 km s^{-1} , this set disappears beyond 350 pc. On the other hand a new set with heliocentric velocities smaller than 0 km s^{-1} appears beyond 300 pc. Could this kinematic transition at 300–350 pc be connected to the expansive movement of the backside of the Lower Centaurus–Crux feature being countered by an opposite motion? The expansion has ceased at about 350 pc and the counter motion halting the expansion is first noticed at about 300 pc.

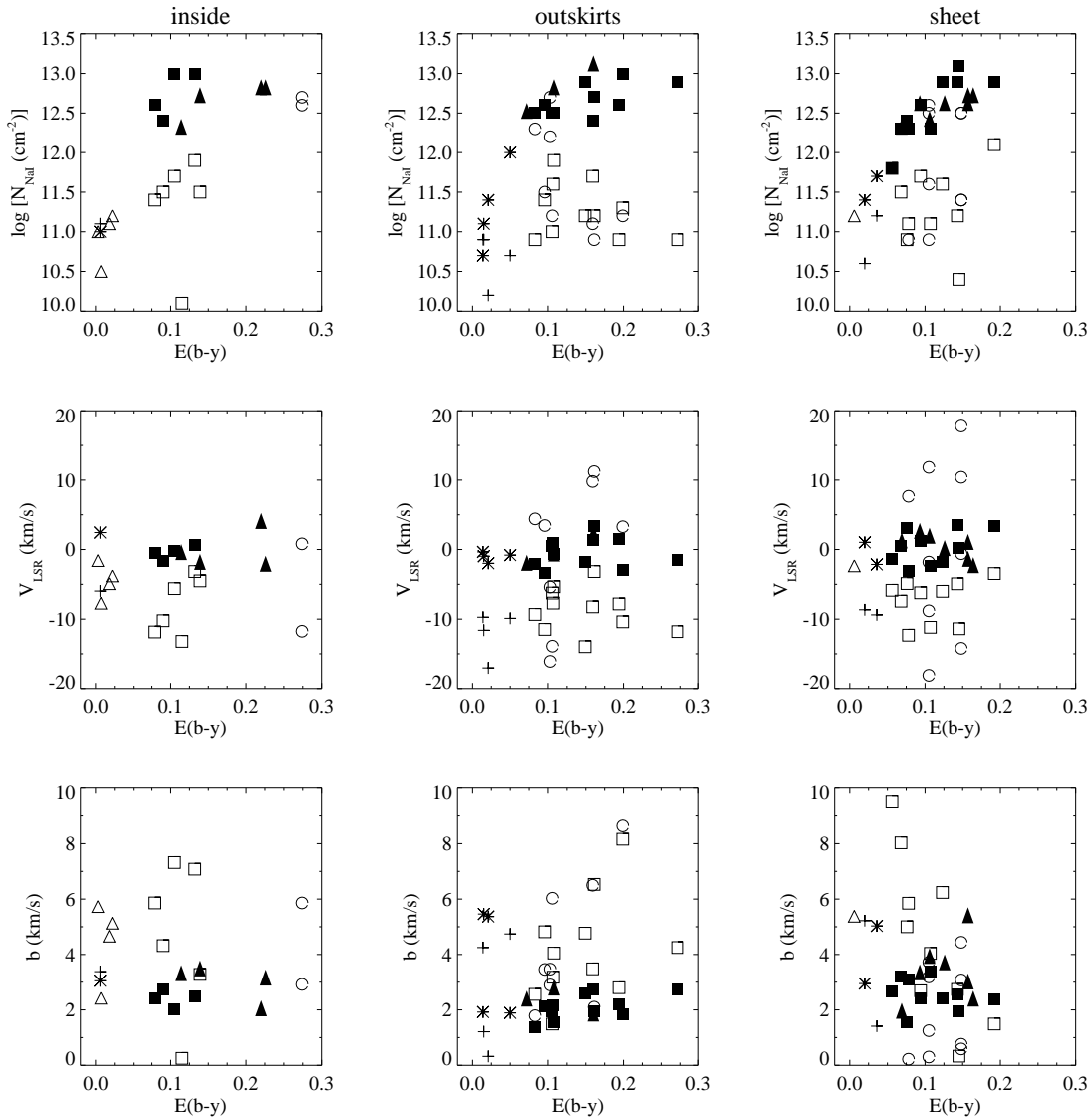


Figure 7. Plots of $\log N_{\text{NaI}}$, V_{LSR} and b against the $E(b-y)$ colour excess. From left to right the columns show the stars with line-of-sight *inside* the clouds' contours, in their *outskirts*, and towards the *sheet*. The plotting symbols have the same meaning as in Fig. 6. The *strong* component is only picked up by the reddened stars, whereas the *weak* component is picked up by both reddened and unreddened stars. Such diagrams suggest that dust and gas apparently have the same distribution along the line of sight

6.2 The interface between the Local and Loop I bubbles

A soft X-ray shadow has recently been discovered on the edges of the Loop I Bubble, cast by a warped annular volume of dense neutral matter that supposedly formed during its collision with the Local Bubble (Egger & Aschenbach 1995). The shadow counterpart, a huge HI ring was also identified on the Dickey & Lockman (1990) data.

Egger & Aschenbach (1995) suggested that the steep increase of the column density caused by the annular feature, from less than 10^{20} to $\geq 7 \times 10^{20}$, occurs at a distance of ≈ 70 pc from the Sun. This distance is thought to be supported by results from optical and UV spectral analysis of stars near the center of Loop I ($310^\circ \leq l \leq 330^\circ$ and $15^\circ \leq b \leq 25^\circ$) by Centurion & Vladilo (1991), who found the presence of a neutral gas wall of $N_{\text{H}} \sim 10^{20} \text{ cm}^{-2}$ at a distance of 40 ± 25 pc. See also the determination of the radial extent of the Local Hot Bubble recently estimated by

Snowden et al. (1998) based on the *ROSAT* and *IRAS* all-sky survey data.

However, for the hydrogen column density of the annular feature, the colour excess and the NaI column densities obtained in this work suggest that the interaction zone between the two bubbles is located around 120-150 pc from the Sun. This result is corroborated by Sfeir et al. (1999) – an improved version of the 3D mapping of the Local Bubble cavity has been recently obtained by Lallement et al. (2003) – where it is found that for the region investigated here the 20–50 mÅ isocontours at $b \sim -20^\circ$ occurs at $d \approx 100 - 150$ pc, but at $b \sim -45^\circ$ the distance is close to 70 pc. The hydrogen column densities and velocities observed by Centurion & Vladilo (1991) are more consistent with our lower column density component at $d \leq 60$ pc. In the same strip of latitude, the wall of neutral gas has a column density $N_{\text{H}} \sim 10^{21} \text{ cm}^{-2}$, as suggested by Iwan (1980). Moreover, the hydrogen column densities towards the interaction ring, used by Egger & Aschenbach

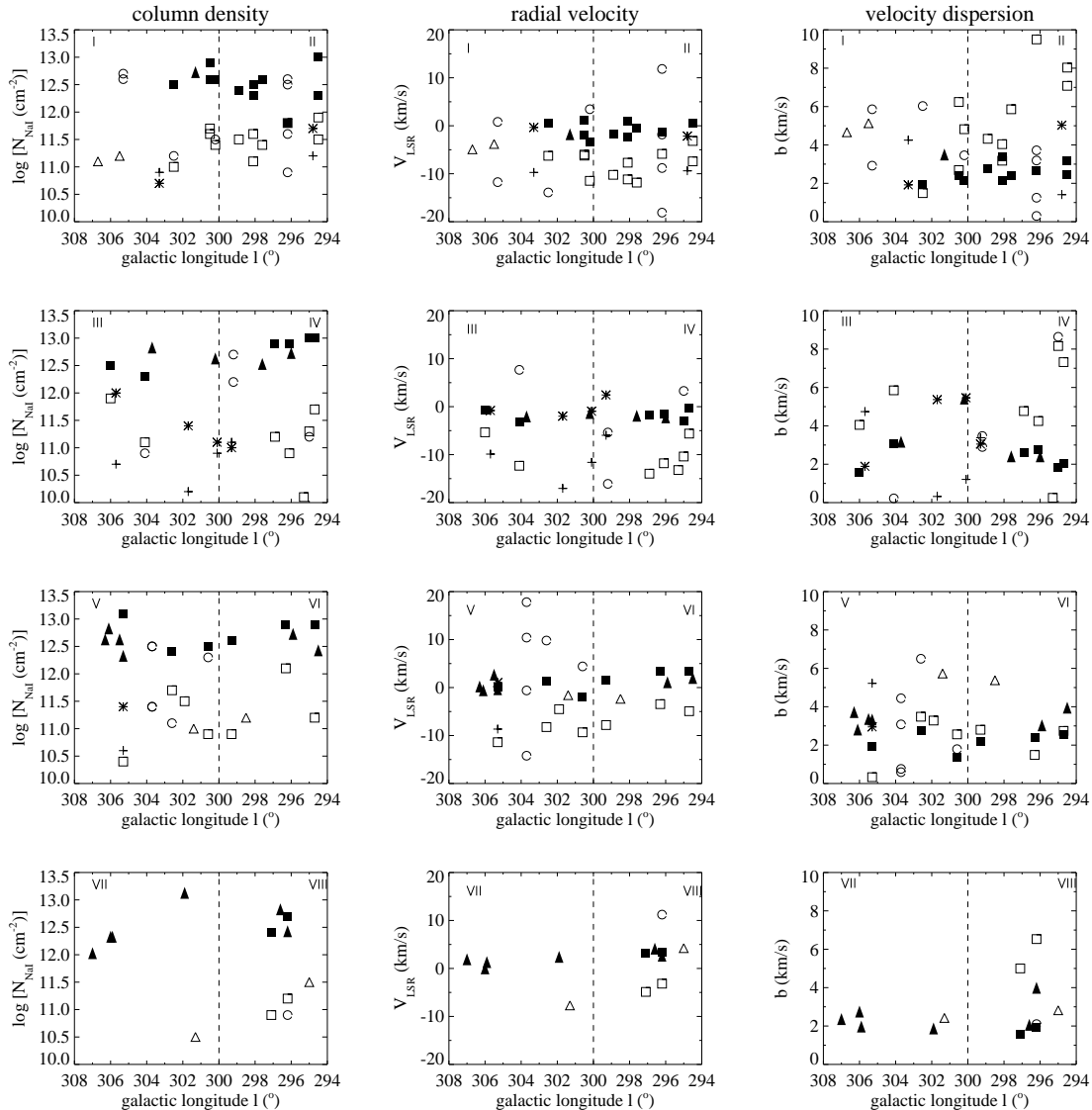


Figure 8. a Distribution of $\log N_{\text{NaI}}$ (left), V_{LSR} (middle) and b (right) with the Galactic Longitude. The symbols have the same meaning as for Fig. 6 and the dashed lines indicate the dividing point between the sub-areas. The *weak* and the *strong* components form two extended interstellar components, that cover the whole connecting area. There seems to have no dependence with the Galactic longitude, but the radial velocity may be increasing with the latitude

(1995, cf. their Fig. 4) suggest a value around $3 \times 10^{19} \text{ cm}^{-2}$ at 70 pc, also more consistent with our nearby feature. Since Centurion & Vladilo (1991) have observed only unreddened directions our results cast some doubt on the distance to the interaction zone being located around 70 pc. It seems that the annular region is twisted and folded, with different directions having different distances.

In addition to the velocities indicative of the flow of material in the last section, some of the more distant stars also have components at nearly 0 km s^{-1} in the LSR (Frisch & York 1986). In the longitude range $360 \leq l \leq 345$ there are a number of low velocity ($-4 \leq V_{\text{LSR}} \leq +4 \text{ km s}^{-1}$) components with generally strong Na I lines, consistent with the proximity of the ρ Oph and Lupus clouds (Crawford 1991). In the longitude range $325 \leq l \leq 295$ there are also several components, in the positive latitudes, with LSR velocities which are small but clearly negative ($-4 \leq V_{\text{LSR}} \leq 0 \text{ km s}^{-1}$).

As mentioned in Sect. 5, the feature around 120 – 150 pc observed in our work, has column densities suggesting that the gas is

associated to the dust sheet observed towards the Coalsack, Musca and Chamaeleon direction. It is certainly not appropriate to make generalizations exclusively from our data, but the fact that the velocities observed here are also in the same range ($-3 \leq V_{\text{LSR}} \leq +3 \text{ km s}^{-1}$), suggests that the dust and gas feature around 120 – 150 pc, seems to be part of an extended large scale feature of similar kinematic properties, supposedly identified with the interface of the Local and Loop I bubbles.

7 CONCLUSIONS

The investigation of the interstellar gas components towards the Southern Coalsack, Chamaeleon and Musca dark have produced the following results:

- The interstellar gas is distributed in two extended sheet-like

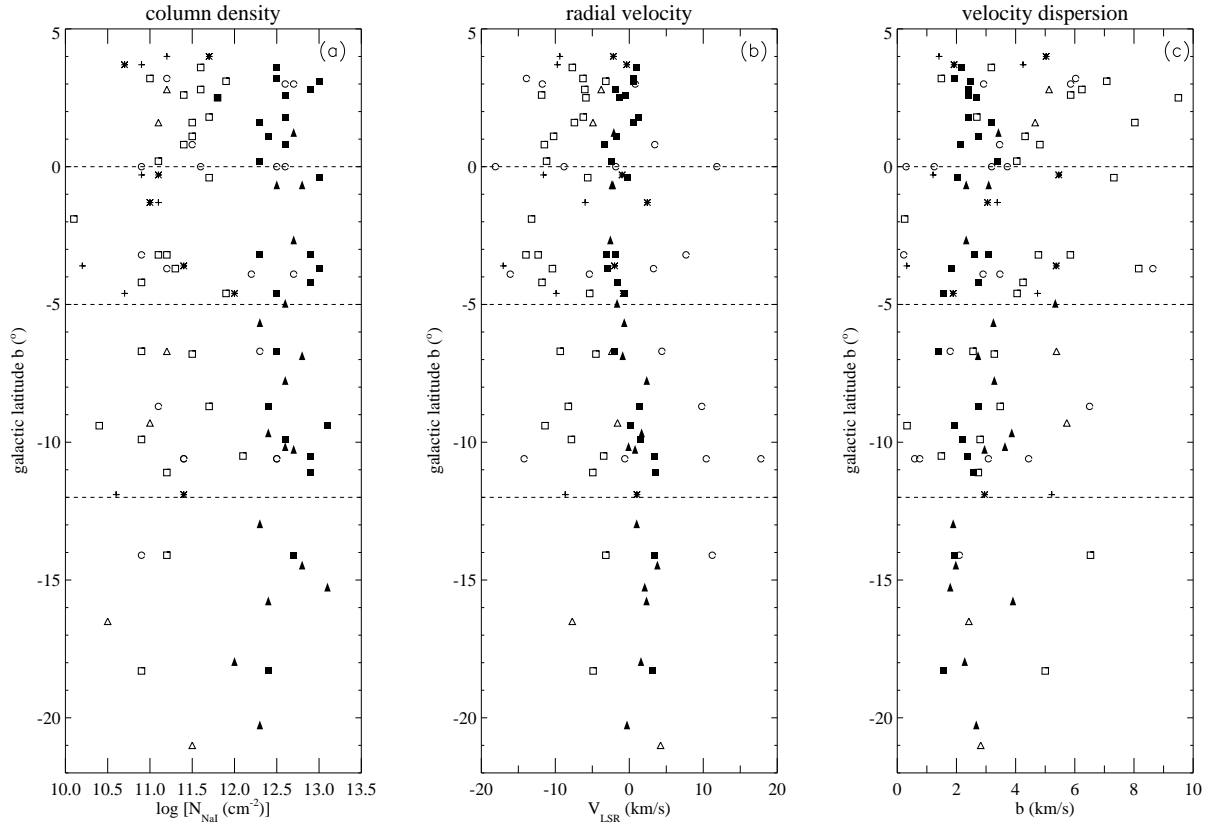


Figure 8. Distribution of $\log N_{\text{Na I}}$ (left), V_{LSR} (middle) and b (right) with the Galactic Latitude. The symbols have the same meaning as for Fig. 6 and the horizontal dashed lines indicate the dividing point between the sub-areas. The *weak* and the *strong* components are present in the whole latitude range. Note that radial velocity of the *strong* component seems to increase from -3 km s^{-1} near the galactic plane to $+3 \text{ km s}^{-1}$ near the southern parts

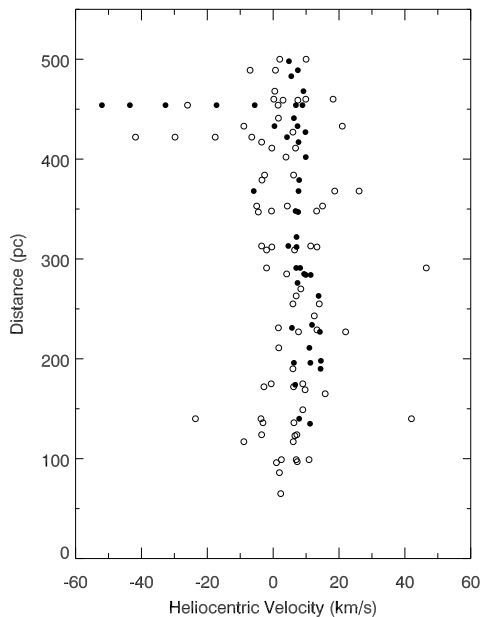


Figure 9. Heliocentric velocities of the interstellar clouds components as a function of stellar distance. Filled circles represent components for which $\log N_{\text{Na I}} \geq 12.5 \text{ cm}^{-2}$, while open circles represent components for which $\log N_{\text{Na I}} < 12.5 \text{ cm}^{-2}$. Note the well defined velocity distribution for the *strong* component and that it appears for stars beyond $\sim 140 \text{ pc}$.

structures permeating the whole searched area, one at $d \leq 60 \text{ pc}$ and another around $120 - 150 \text{ pc}$ from the Sun.

- The nearby feature is approaching to the Sun with average radial velocity of -7 km s^{-1} , has low average column density $\log N_{\text{Na I}} \approx 11.2 \text{ cm}^{-2}$ and has velocity dispersion $b \approx 5 \text{ km s}^{-1}$. The more distant feature has column densities between $12.3 \leq \log N_{\text{Na I}} \leq 13.2$, average velocity dispersion $b \approx 2.5 \text{ km s}^{-1}$ and seems associated to the dust sheet observed towards the Coalsack, Musca and Chamaeleon direction. Its velocity is centered around 0 km s^{-1} , but there is a trend for increasing from -3 km s^{-1} near $b = 1^\circ$ to 3 km s^{-1} near $b = -18^\circ$.

- In agreement with several independent investigations the nearby low column density feature indicates a general outflow from the Sco-Cen association, while the dust and gas feature around $120 - 150 \text{ pc}$ seem to be part of an extended large scale feature of similar kinematic properties, supposedly identified with the interaction zone of the Local and Loop I bubbles. Assuming that the interface and the ring-like volume of dense neutral matter have similar properties, our results suggest that the interaction zone between the bubbles is twisted and folded.

ACKNOWLEDGMENTS

This paper is based on observations collected at the European Southern Observatory (ESO, La Silla, Chile). The staff at ESO, both in La Silla and Garching are thanked for the assistance during the observing runs. Dr. Welty is thanked for the line-fitting program

and Dr. Egger is thanked for the ring-like feature contours. The Brazilian Agencies CNPq and FAPEMIG, and the Danish NBIfAFG are acknowledged for supporting this research. W. Corradi wishes to express his gratitude to the NBIfAFG members for the invaluable help during the development of this work in Denmark.

REFERENCES

- Bochkarev N.G., 1987, *Ap&SS*, 138, 229
 Bowyer S., Lieu R., Sidher S.D., et al., 1995, *Nat*, 375, 212
 Breitschwerdt D., Freyberg M.J., Egger R., 2000, *A&A*, 361, 303
 Bruhweiler F.C., 1996 In: Bowyer S., Malina R.F. (eds.) *Proc. IAU Colloq. 152, Astrophysics in the Extreme Ultraviolet*. Kluwer, Dordrecht, p. 261
 Centurion M., Vladilo G., 1991, *ApJ*, 372, 494
 Cha A.N., Sahu M.S., Warren Moos H, Blaauw, A., 2000, *ApJS*, 129, 281
 Corradi W.J.B., Franco G.A.P., 1995, *A&AS*, 112, 95
 Corradi W.J.B., Franco G.A.P., Knude J., 1997, *A&A*, 326, 1215 (Paper I)
 Cox D.P., Reynolds R.J., 1987, *ARA&A*, 25, 303
 Cowie L.L., Songaila A, 1986, *ARAA*, 24, 499
 Cravens T.E., 2000, *ApJ*, 532, 153
 Crawford I.A., 1991, *A&A*, 247, 183
 Crutcher R.M., 1982, *A&A*, 254, 82
 Dame, T.M., Ungerechts, H., Cohen, R.S., de Geus, E.J., et al. , 1987, *ApJ*, 322, 706
 de Geus E.J., 1992, *A&A*, 262, 258
 Dickey J.M., Lockman F.J., 1990, *ARA&A*, 28, 215
 D’Odorico S., Ghigo M., Ponz D., 1987 In: *An Atlas of the Thorium Argonium Spectrum for the ESO Echelle Spectrograph in the λ 3400 – 9000 Å Region*, European Southern Observatory
 Egger R.J., Aschenbach B., 1995, *A&A*, 294, L25
 ESA, 1997, *The Hipparcos and Ticho Catalogues*, ESA SP-1200. ESA Publications Division, Noordwijk
 Feitzinger J.V., Stüwe J.A., 1984, *A&AS*, 58, 365 (erratum: 63, 203)
 Ferlet R., Vidal-Madjar A., Gry C., 1985, *ApJ*, 298, 838
 Franco G.A.P., 1989, *A&A*, 215, 119
 Franco G.A.P., 1991, *A&A*, 251, 581
 Frisch P.C., York D.G., 1983, *ApJ*, 271, L59
 Frisch P.C., York D.G., 1986 In: Smoluchowski R., Bahcall J.N., Matthews M.S. (eds.) *The Galaxy and the Solar System*. University of Arizona Press, Tucson, p. 83
 Gehrels N., Chen W., 1993, *Nat*, 361, 706
 Génova R., Beckman J.E., Bowyer S., Spicer T., 1997, *ApJ*, 484, 761
 Hartquist, T.W., 1994, *Ap&SS*, 216, 185
 Hobbs L.M., 1978, *ApJ*, 222, 491
 Howarth I.D., Phillips A.P., 1986, *MNRAS*, 222, 809
 Iwan D., 1980, *ApJ*, 169, 25
 Kaper L., Pasquini L., B., 1996, In: “CAT/CES Operating Manual”
 Kerp J., Herbstmeier U., Mebold U., 1993, *A&A*, 268, L21
 Knude J., 1978, In: Reiz A., Andersen J. (eds.) *Astronomical Papers dedicated to B. Strömgren*. Copenhagen Univ. Obs., Copenhagen, p. 273
 Lallement R., 1998, *Lectures Notes in Physics*, 506, 19
 Lallement R., Bertin P., 1992, *A&A*, 266, 479
 Lallement R., Ferlet R., Lagrange A.M., Lemoine M., Vidal-Madjar A., 1995, *A&A* 304, 461
 Lallement R., Vidal-Madjar A., Ferlet R., 1986, *A&A*, 168, 225
 Lallement R., Welsh B.Y., Vergely J.L., Crifo F., Sfeir D., 2003, *A&A* – in press
 Mihalas, D., Binney J., 1981, In “Galactic Astronomy” 2nd edition (San Francisco, Freeman)
 Nyman L.-Å., Bronfman L., Thaddeus P., 1989, *A&A*, 216, 185
 Paresce F., 1984, *AJ*, 89, 1022
 Redfield S., Linsky J.L., 2000, *ApJ*, 534, 825
 Sembach K.R., Danks A.C., Savage B.D., 1993, *A&AS*, 100, 107
 Snowden S.L., Cox D.P., McCammon D., Sanders W.T., 1990, *ApJ*, 354, 211
 Snowden S.L., Mebold U., Hirth W., Herbstmeier U., Schmidt J.H.M.M., 1991, *Sci*, 252, 1529
 Snowden S.L., Freyberg M.J., Plucinsky P.P., et al., 1995, *ApJ*, 454, 643
 Snowden S.L., Egger R., Finkbeiner D.P., Freyberg M.J., Plucinsky P.P., 1998, *ApJ*, 493, 715
 Savage B.D., Bohlin R.C., Drake J.F., et al., 1977, *ApJ*, 216, 291
 Spitzer, Jr., L.: 1978, “Physical processes in the interstellar medium” (New York: John Wiley & Sons)
 Sfeir D.M., Lallement R., Crifo F., Welsh B.Y., 1999, *A&A*, 346, 785
 Tinbergen J., 1982, *A&A*, 105, 53
 Wang Q.D., Yu K.C., 1995, *AJ*, 109, 698
 Warwick R.S., Barber C.R., Hodgkin S.T., Pye J.P., 1993, *MNRAS*, 262, 289
 Weaver H., 1979 In: Burton W.B. (ed.) *Proc. IAU Symp. 84, Large-Scale Characteristics of the Galaxy*. Reidel, Dordrecht, p. 295
 Welsh B.Y., Vedder P.W., Vallerga J.V., 1990, *ApJ*, 358, 473
 Welsh B.Y., Vedder P.W., Vallerga J.V., Craig N., 1991, *ApJ*, 381, 462
 Welsh B.Y., Craig N., Vedder P.W., Vallerga J.V., 1994, *ApJ*, 437, 638
 Welty D.E., Hobbs L.M., Kulkarni V.P., 1994, *ApJ*, 436, 152